The Astrophysical Journal, 975:68 (18pp), 2024 November 1 https://doi.org/10.3847/1538-4357/ad794d

A View of the Long-term Spectral Behavior of Ultracompact X-Ray Binary 4U 0614+091

D. L. Moutard[1,2], R. M. Ludlam[1], E. M. Cackett[1], J. A. García[3], J. M. Miller[2], and D. R. Wilkins[4]
[1] Department of Physics & Astronomy, Wayne State University, 666 West Hancock St, Detroit, MI 48201, USA; moutard@umich.edu
[2] Department of Astronomy, University of Michigan, 1085 S. University, Ann Arbor, MI 48109, USA
[3] Cahill Center for Astronomy and Astrophysics, California Institute of Technology, 1200 E. California Blvd, MC 290-17, Pasadena, CA, 91125, USA
[4] Kavli Institute for Particle Astrophysics and Cosmology, Stanford University, 452 Lomita Mall, Stanford, CA 94305-4085, USA
Received 2024 July 24; revised 2024 September 4; accepted 2024 September 9; published 2024 October 25

Abstract

In this study, we examine 51 archival NICER observations and six archival NuSTAR observations of the neutron star ultracompact X-ray binary (UCXB) 4U 0614+091, which span over 5 yr. The source displays persistent reflection features, so we use a reflection model designed for UCXBs, with overabundant carbon and oxygen (XILLVERCO) to study how various components of the system vary over time. The flux of this source is known to vary quasiperiodically on a timescale of a few days, so we study how the various model components change as the overall flux varies. The flux of most components scales linearly with the overall flux, while the power law, representing coronal emission, is anticorrelated, as expected. This is consistent with previous studies of the source. We also find that during observations of the high-soft state, the disk emissivity profile as a function of radius becomes steeper. We interpret this as the corona receding to be closer to the compact object during these states, at which point the assumed power law illumination of XILLVERCO may be inadequate to describe the illumination of the disk.

Unified Astronomy Thesaurus concepts: X-ray binary stars (1811); Neutron stars (1108); High energy astrophysics (739); Accretion (14)

1. Introduction

In low-mass X-ray binary (LMXB) systems, a neutron star (NS) or black hole (BH) typically interacts with a main sequence star $\lesssim 1\ M_{\odot}$. This interaction takes place via Roche lobe overflow, where the stellar companion fills its Roche lobe until the material begins to fall toward the NS or BH and eventually circularizes into an accretion disk. Typical LMXBs have orbital periods on the timescales of hours or days, but some display a much shorter orbital period (A. Avakyan et al. 2023). This subclass of LMXB is called an ultracompact X-ray binary (UCXB) and is generally composed of an NS or BH and an H-poor degenerate companion like a white dwarf (WD) or He star. The orbital period required to be considered a UCXB is typically < 80 minutes, which would not be possible for larger main sequence or H-rich stars without directly colliding with the compact accretor (G. J. Savonije et al. 1986; A. Bahramian & N. Degenaar 2023). Because UCXB companion stars are chemically distinct from a main sequence star, the abundances in the accretion disk will also differ quite greatly from those of LMXBs which are not ultracompact. These systems typically have negligible amounts of hydrogen and an overabundance of oxygen (G. Nelemans et al. 2004, 2006). Aside from being useful avenues for studying accretion physics and probing the nature of compact objects in a unique way, these sources will also produce gravitational waves on the order of mHz. This will be detectable by future multimessenger missions such as LISA (W.-C. Chen et al. 2020), so understanding and classifying these systems well in advance is useful.

LMXB systems are typically defined as having a few primary components. These are a disk that produces thermal X-rays (N. I. Shakura & R. A. Sunyaev 1973), a corona close to the compact object that produces hard, nonthermal X-rays via the Compton scattering of disk photons, and in the case of NS systems, thermal photons from the NS itself (R. A. Syunyaev et al. 1991). These contribute to the overall continuum of the X-ray spectrum, but coronal photons will also illuminate the disk and be reprocessed by the material therein. This leaves a signature as the photons are reprocessed, often in the form of a relativistically broadened iron K-shell fluorescence emission around 6–7 keV (A. C. Fabian et al. 1989). In the case of UCXBs, the overabundance of oxygen means that this feature may be screened as interactions occur more readily with more abundant elements in the disk, and instead, a more dominant O VIII feature appears in the softest X-rays at around 0.67 keV (F. Koliopanos et al. 2013, 2021). These additional features are considered part of the reflection spectrum and are believed to come from the innermost region of the disk (Y. Tanaka et al. 1995; S. Bhattacharyya & T. E. Strohmayer 2007). Based on the broadening of these lines, we can determine several useful quantities, such as the location of the inner disk with respect to the compact object and the inclination of the system.

One such UCXB is 4U 0614+091. This source was discovered in 1978 by the Uhuru mission and is considered to be a binary system (J. H. Swank et al. 1978). Later observations of type I X-ray bursts determined that the compact object was an NS (S. Brandt et al. 1992), followed by later spectral studies verifying the presence of elements that make the companion likely to be WD (A. M. Juett et al. 2001; G. Nelemans et al. 2004). The orbital period was measured by T. Shahbaz et al. (2008) using optical data to be approximately 50 minutes. This was done by directly observing modulations in the optical light curve caused by the uneven heating of the donor star.

D. L. Moutard et al. (2023) used reflection modeling to study 4U 0614+091 as the flux changed. The reflection model used

therein is XILLVERCO, which is a modification of the XILLVER reflection table (J. García et al. 2013). The key difference is that XILLVERCO has abundances designed for CO WD, with reduced amounts of hydrogen and helium (O. K. Madej et al. 2014). The source appears to have a quasiperiodic flux, varying on the timescale of ∼a week. The study concluded that the flux of most of the spectral components is correlated with the overall flux but found that in the lowest flux state, the nonthermal flux was at its highest, and the disk appeared to truncate to about twice the innermost stable circular orbit ($R_{\rm ISCO}$). $R_{\rm ISCO}$ is the closest a particle can stably orbit a compact object before falling onto it and is equal to 6 R_g ($R_g = GM/c^2$, with 6 $R_g = 12.4$ km for a nonrotating 1.4 $M_\odot$ NS). A parallel is drawn to BH-LMXB systems, where typically at lower luminosities the disk truncates (C. Done et al. 2007). The trend is less clear in NS systems, as the complicated magnetic fields affect the location of the inner disk, but since both NSs and BHs are compact accretors, this comparison is not unwarranted.

In this paper, we extend the study from D. L. Moutard et al. (2023), supplementing the four NICER observations with additional archival observations. Our goal is to study the long-term behaviors of the system as the overall flux varies and to test further analogies between NS and BH accretion systems. While the previous study benefited from simultaneous NICER and NuSTAR observations, the observations only cover roughly one period of the quasiperiodic flux oscillations. Because of this, it is difficult to draw conclusions about the system more generally. By extending the study, we are able to draw more robust conclusions about model parameters and their relation to the variation in flux over time. This will also serve as a test of the limits of XILLVERCO. The model currently assumes the bulk of the illumination is from the nonthermal corona, but it is well understood that in higher luminosity states, the continuum shifts to be dominated by softer thermal X-rays (D. Lin et al. 2007). We choose NICER because of the large number of archival observations. NICER also provides excellent coverage in the band containing the O VIII feature, which is key to understanding UCXBs. We also supplement this with six archival NuSTAR observations. NuSTAR can be useful for constraining the overall continuum shape, as the band extends into the hard X-rays. Although there are many observations of 4U 0614+091 using Swift, the source is quite bright. Therefore, the observations are taken in windowed mode to account for additional photon pileup. These pileup effects can introduce additional uncertainties to the emission spectrum of a source (J. M. Miller et al. 2010; C. Ng et al. 2010), so we opt to use NICER and NuSTAR, which do not suffer from such pileup effects. These instruments also allow us to directly compare to our previously published literature. Section 2 of this paper discusses the details of the archival observations and the selection criteria, Section 3 provides details on the modeling and reports the relevant results of fitting spectra to these models, and Section 4 discusses the physical interpretations of these results. Section 5 summarizes this work.

2. Observations and Data Reduction

To study 4U 0614+091 we primarily use archival NICER observations because the large number available makes it possible to extend this study over the course of several years. We limited archival NICER observations to those with >5 ks before filtering, leaving us with 51 total observations. This exposure cut is chosen to guarantee all observations (regardless of state) have above 10^6 total counts, ensuring comparable data quality to even the lowest flux observations from D. L. Moutard et al. (2023). We then calibrate all of these observations using NICERDAS 2023-08-22_v011a and CALDB 20221001. This is done by first using NICERL2 for geomagnetic prefiltering, then followed by NIMAKETIME with COR_SAX >4.0 to manage particle overshoots and KP <5 to filter out high particle background. We then construct good time intervals (GTIs) using NIEXTRACT-EVENTS. To construct spectra, backgrounds, and responses, we use NICERL3-SPECT with the 3C50 background model. We bin the spectra using the optimal binning scheme with a required count rate of 30 counts per bin to ensure χ^2 statistics are valid (J. S. Kaastra & J. A. M. Bleeker 2016). We construct light curves using NICERL3-LC, which normalizes the light curves to the number of active detectors. These light curves are generated using several X-ray bands, including the total band (0.5–6.8 keV), the super soft band (0.5–1.1 keV), the soft band (1.1–2.0 keV), the intermediate band (2.0–3.8 keV), and the hard band (3.8–6.8 keV). We compile these light curves into hardness–intensity and color–color diagrams (Figure 1), which demonstrate that the hard color of this system is largely unchanged over the course of observations. One observation, observation ID (obsid)= 1050020115, contained a type I X-ray burst, which was filtered out using a custom GTI. The observation date of all 51 NICER observations is shown

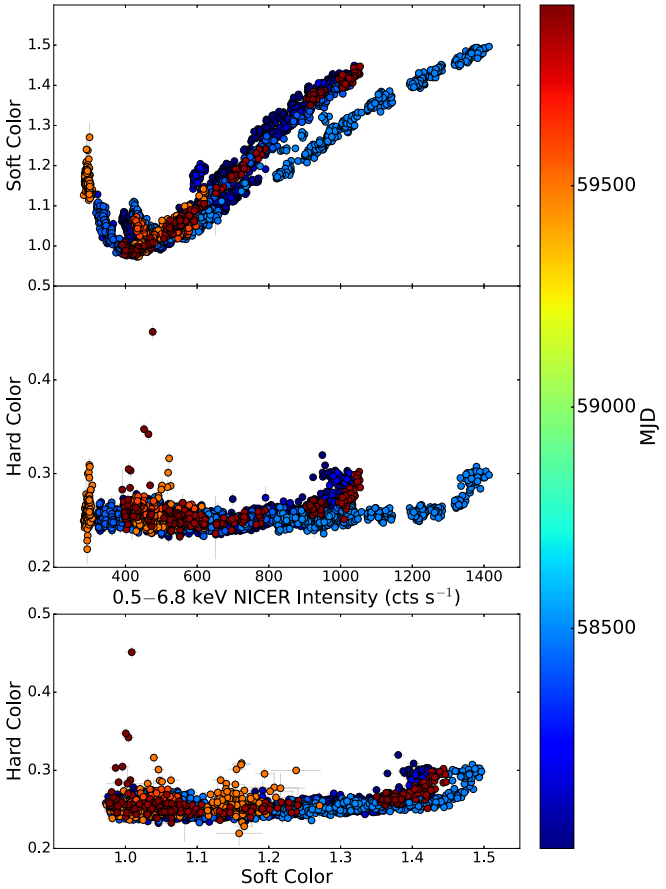

Figure 1. The hardness–intensity diagram for the soft color (1.1–2.0 keV/0.5–1.1 keV) and the hard color (3.8–6.8 keV/2.0–3.8 keV), as well as the color–color diagram for all 51 observations. The observations are binned into 150 s segments for clarity. We see that the hard color stays relatively constant throughout all observations, but the soft color varies more distinctly over time.

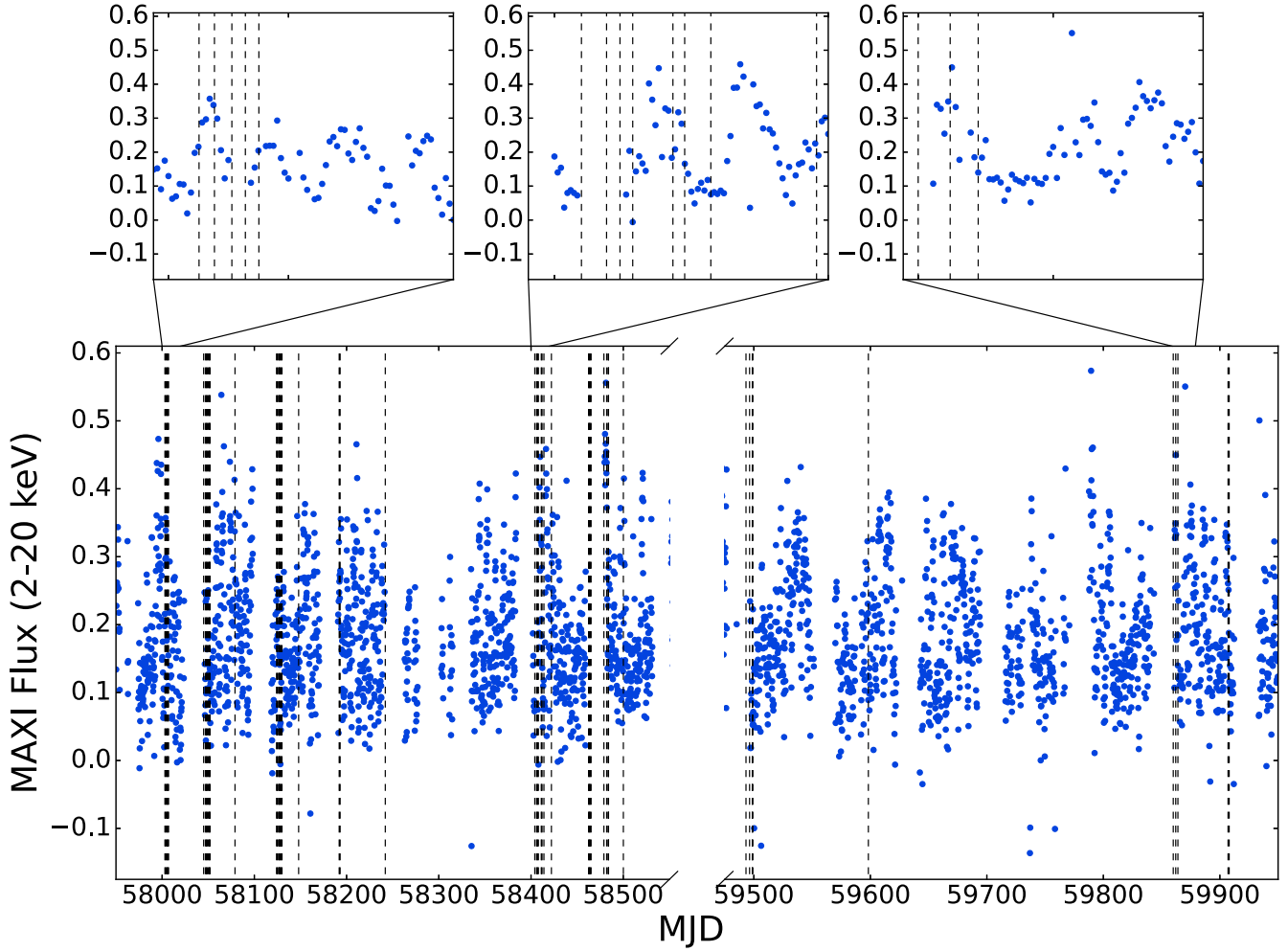

Figure 2. Long-term MAXI light curve in blue points with the start date of each observation overlaid as dashed lines. The top row of plots highlights specific 20 days regions of the light curve, demonstrating that the source is captured in various states. These zoomed-in plots also display the quasiperiodic nature of the flux of the source.

overlaid on a long-term MAXI light curve in Figure 2, with insets that display 20 day intervals.

We also look at six NuSTAR observations of 4U 0614+091. These are generated by first defining source regions in a 100″ circle centered on the source, and another 100″ circle centered off the source to define a background region using ds9. The reduction of these observations is done using NUSTARDAS v2.1.2 and CALDB 20230816. More information on all observations can be seen in Table A1 in Appendix A. We plot the NuSTAR light curves using 1 s time bins and detect no bursts in any observation, so no further filtering was done.

3. Results and Analysis

In this section we describe the specifics of the models used in this work to study the reflection spectrum. We begin by first modeling only the continuum components, then proceed to add a reflection component to the model.

3.1. NICER Continuum Modeling

Before using reflection models, we first test a continuum model similar to the one used in D. L. Moutard et al. (2023). The models are constructed and fit in XSPEC VER. 12.13.1 (K. A. Arnaud 1996). The first component is TBABS, a multiplicative model component used to measure absorption due to neutral hydrogen in the interstellar medium (ISM), using the WILM cross section (J. Wilms et al. 2000) and the VERN cross section (D. A. Verner et al. 1996). This is followed by two multiplicative absorption edges to manage features at ∼0.4 and ∼0.9 keV, which can interfere with the O VIII line. These features are potentially astrophysical in origin, owing to the ISM along the line of sight (C. Pinto et al. 2013). The inclusion or exclusion of these edges may interfere with measurements of the O VIII feature. For the sake of consistency with D. L. Moutard et al. (2023), we continue this analysis with two edges, but we discuss the implications further in Section 4.4. The higher and lower energy edges roughly correspond to the Fe L and C K edges, respectively, though the edge at lower energy has a centroid that sits near or below the band used, so it is less confidently measured. We are deferring to previous studies of this source and similar sources that use such edges (O. K. Madej et al. 2014; R. M. Ludlam et al. 2020; D. L. Moutard et al. 2023). After fully modeling the spectra (see Section 3.2 for more details), we find the edges have average energies at ∼0.40 and ∼0.87 keV, with respective optical depths of ∼0.85 and ∼0.18. The lower energy edge is roughly consistent with a known nitrogen detector edge, while the higher energy edge sits in the region of an Fe L or

Ne K edge. The remaining model components are BBODY to account for thermal emission from the NS, DISKBB to account for thermal emission from the disk, and CUTOFFPL to account for the nonthermal emission from the corona. We use CUTOFFPL rather than a standard POWERLAW because many observations in the high–soft state display a high energy cutoff within the bands observed (N. Degenaar et al. 2018). Using this while allowing the cutoff energy to increase beyond the band provided by NICER allows us to account for spectra both with and without this energy cutoff, allowing our model to be agnostic to the spectral state. The final model used to fit the continuum is TBABS*EDGE*EDGE*(BBODY+DISKBB+CUTOFFPL). All of the models are fitted in the 0.45–9 keV range for consistency with D. L. Moutard et al. (2023).

With the model in place, we proceed to fit all 51 NICER spectra. We use χ^2 statistics with Churazov weighting. Churazov weighting is similar to standard χ^2 statistics, but takes into account adjacent bins to help prevent overfitting (E. Churazov et al. 1996). However, this can also lead to higher values of χ^2 statistics. If we were using standard weighting, the reduced χ^2 values reported would often be above acceptable levels, but the values found in this analysis are consistent with those from D. L. Moutard et al. (2023). With the fit in place, we then calculate the errors on continuum parameters by using the fitted model as a starting point for a Markov Chain Monte Carlo fit with 100 walkers, a burn-in of 100,000, and a chain length of 10,000. This is done using the CHAIN command in XSPEC. To demonstrate the quality of these fits, we show a histogram of reduced χ^2 values in Figure 3, and compare the continuum-only model to a model with a reflection component added (as discussed in Section 3.2). The inclusion of the reflection component leads to an improvement of in χ^2 values of ∼1566 for 6 degrees of freedom (dof). A table of all continuum values can be found in Appendix B in Table B1. An example of three unfolded NICER spectra can be seen in Figure 4, demonstrating the various states in which the source is observed.

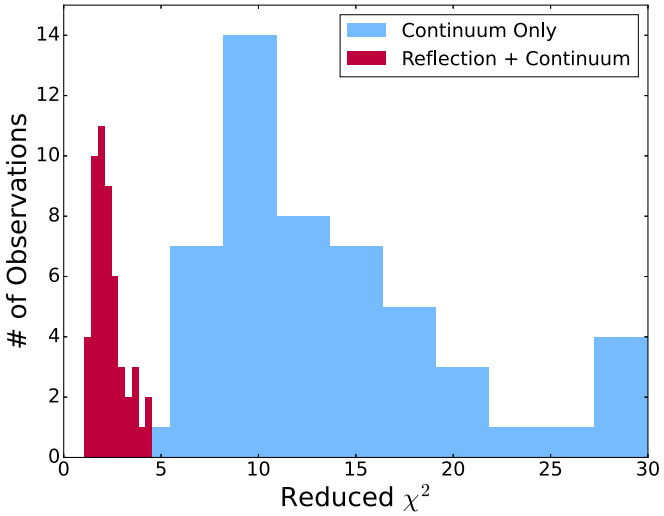

Figure 3. A comparison of the reduced χ^2 values for the observations when fit only with a continuum vs. when fit with a reflection component. We see that a reflection component significantly improves the reduced χ^2 statistics for all observations. This should not be understood as a robust statistical comparison of the models but rather as a quick reference to determine whether a reflection component significantly improves the fit quality. The values shown here correspond to an average χ^2 improvement of ∼1566 for the additional 6 dof. Note: the two models are binned differently for readability.

3.2. NICER Reflection Modeling

With the continuum models in place we then proceed to add a reflection component. This reflection component is modeled using RELCONV*XILLVERCO. As mentioned previously, XILLVERCO is an adaptation of XILLVER with high carbon and oxygen abundances to account for UCXB features. RELCONV is a relativistic convolution kernel that accounts for the broadening of the features in XILLVERCO. In RELCONV we tie the two emissivity indices $q_1 = q_2 = q$. This makes the parameter $R_{\rm BR}$ redundant, so we fix it to 500 R_g. Since we are dealing primarily with the inner disk region, we also fix the outer radius to 990 R_g, as we do not expect this parameter to affect our results. We fix the dimensionless spin parameter a to 0. The limb darkening parameter, used to control whether the model accounts for limb darkening in the source, is also set to 0. This leaves us with three free parameters in RELCONV: q, as mentioned above, the inclination i, and the location of the inner disk radius $R_{\rm in}$, displayed in this paper in units of $R_{\rm ISCO}$. For XILLVERCO and RELCONV, we fix the inclination to 55°; this value is an average of measured values from previous works (O. K. Madej et al. 2014; R. M. Ludlam et al. 2019), and serves to reduce the number of free parameters. The same was done in D. L. Moutard et al. (2023), which found that the parameters do not vary greatly when the inclination is allowed to be free. We tie the power-law index and energy cutoff in XILLVERCO to those from CUTOFFPL. The remaining free parameters are the normalization,[5] the carbon–oxygen abundance $A_{\rm CO}$, the frac parameter, and the temperature $kT_{\rm xill}$. The frac parameter describes the ratio of the illuminating flux from the power law to that of the blackbody, which emerges from the disk at the point of reprocessing. $kT_{\rm xill}$ is the temperature of that emergent blackbody. The ionization $\log \xi$ is not a parameter in XILLVERCO, but can be calculated using

$$\xi = \frac{4\pi}{n} F_x \tag{1}$$

where $F_x = \text{frac} \times \sigma T^4$ with frac being the same as the frac parameter, σ being the Stefan–Boltzmann constant, and T being the temperature from $kT_{\rm xill}$ (J. García et al. 2013). n is the disk number density, which is fixed to 10^{17} cm^{-3} in XILLVERCO.

We add the reflection component to the continuum model, and then fit using XSPEC. In order to calculate errors, we then repeat the process described for the continuum in Section 3.1. We also calculate the fluxes (both overall and for each component) using the multiplicative model component CFLUX once the models are fit. The results of fitting all of these models can be found in Appendix B in Tables B2 and B3. We measure the equivalent width (EW) of the O VIII feature by applying a DISKLINE model component to the continuum model. DISKLINE is a model designed to fit emission features in accretion disks (A. C. Fabian et al. 1989). We fit the spectrum and use the EQWIDTH command in XSPEC to extract the EW and 90% confidence limit errors. We fix the inclination and outer disk radius to the same values used in XILLVERCO, and allow the emissivity index, inner disk radius, line energy, and normalization to be free. We use the same chain method described above to calculate errors, and the results can be found in Table B4. These equivalent widths are consistently around

[5] See T. Dauser et al. (2016) for a detailed explanation of the normalization.

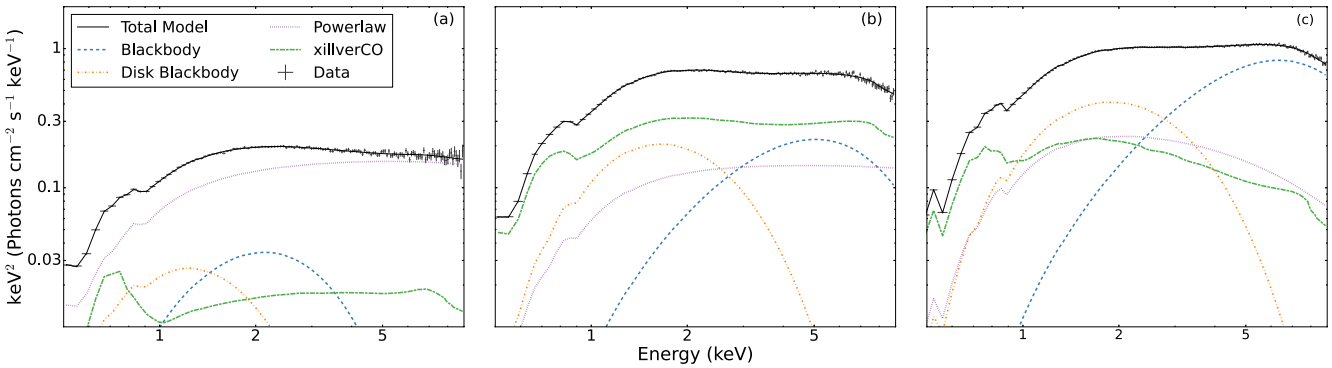

Figure 4. An example of three unfolded NICER spectra with the relevant model components. We show here (a) the lowest flux observation, obsid = 4701010301, (b) an intermediate flux observation, obsid = 1050020236, and the highest flux observation, obsid = 1050020252. These display the range of fluxes we see across these observations, as well as the most relevant components for various fluxes. In (a), we see the power law is dominant and remains relatively flat out to the highest energies, while in (c) the cutoff and preference for a stronger thermal component becomes more apparent. In each, the O VIII feature is visible around 0.7 keV.

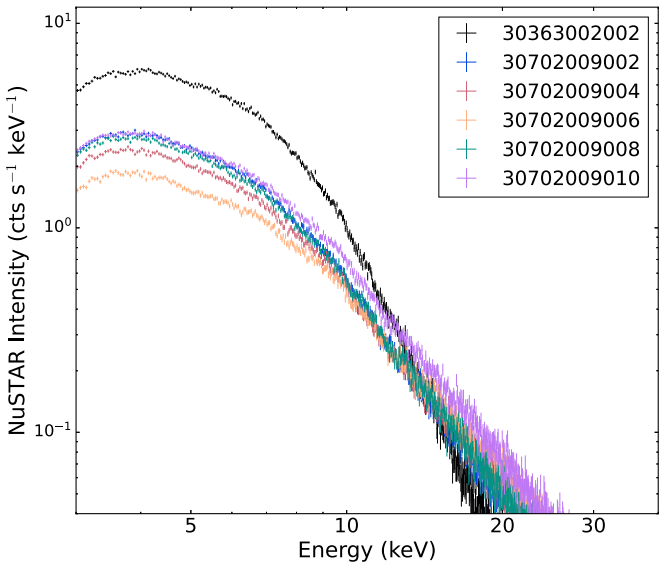

Figure 5. Shown here are the six archival NuSTAR spectra. The five most recent spectra have comparable slopes in the higher energy bands, but the earliest observation, 30363002002, is noticeably different. This means that we cannot effectively use NuSTAR observations that are not simultaneous with NICER observations to constrain continuum parameters for the broader study.

~50 eV, which is similar to the EW of other measured O VIII lines, and is comparable to measured EWs for Fe lines in LMXBs (O. K. Madej & P. G. Jonker 2011; E. M. Cackett et al. 2010). The centroids of these lines are also consistently near 0.7 keV, as anticipated.

3.3. NuSTAR Spectra

We use the six NuSTAR spectra primarily to test whether the high-energy components of the continuum remain constant over time. These spectra unfortunately do not probe the softest regions of the X-ray band. This means they cannot be used to measure the O VIII feature, and so they are used primarily for constraining high-energy continuum features. A similar power-law index was seen in all observations of D. L. Moutard et al. (2023), so we see if this remains true for observations separated further in time. If that were the case, we could use this fact to fix certain parameters, which would be useful in dealing with the large number of spectra involved in this study. However, we see that the slope of the hard X-ray spectrum varies over time (see Figure 5). This means that we cannot use this to constrain and fix the slope of the power-law component, but it does indicate that the spectral state is varying over time.

To study the constraints we can place using the NuSTAR spectra only, we use a similar model to the one described above and model the spectra from 3 to 30 keV, with the spectra binned optimally again with a minimum of 30 counts per bin. This band is chosen to be consistent with D. L. Moutard et al. (2023). The main differences between the model used for the NuSTAR spectra and the NICER spectra are that we omit the EDGE components, as those model features in the low energy, and we add a constant component to account for differences between NuSTAR FPMA and FPMB. The constant is fixed to unity for FPMA and allowed to be free for FPMB. Since TBABS primarily affects the lowest energy bands, we fix the value of $N_{\rm H}$ to 0.4×10^{22} cm^{-2}, an approximate average of the reflection model. We find that the results of certain parameters, such as the power law and the blackbody, are comparable to NICER values and to those in the literature (D. L. Moutard et al. 2023). However, other parameters vary more significantly, with predictions of extremely truncated inner disks, unrealistically low (and sometimes negative) emissivity indices, low $A_{\rm CO}$, and occasionally poorly constrained values from DISKBB. This highlights the utility of instruments with lower energy band passes for UCXB studies and demonstrates the ability of NuSTAR to help constrain continuum parameters. The results of these fits can be found in Table C1 in Appendix C.

4. Discussion

4.1. Flux and Inner Disk Radius

D. L. Moutard et al. (2023) discusses 4U 0614+091 in terms of the overall flux behavior. In that analysis, the flux of all model components scales with the overall flux except the flux of the power-law component, which seems to be anticorrelated. The decrease in the flux of the XILLVERCO component as the illuminating power law increases is explained by a truncated disk during the lowest flux observation. This can also be explained by the fact that the fraction of emitted coronal photons to those reflected decreases as the height of the corona increases. If the coronal height decreases as the source gets softer and the power law becomes weaker, this means more photons illuminate the disk and are reflected, resulting in a greater contribution from XILLVERCO (T. Dauser et al. 2016).

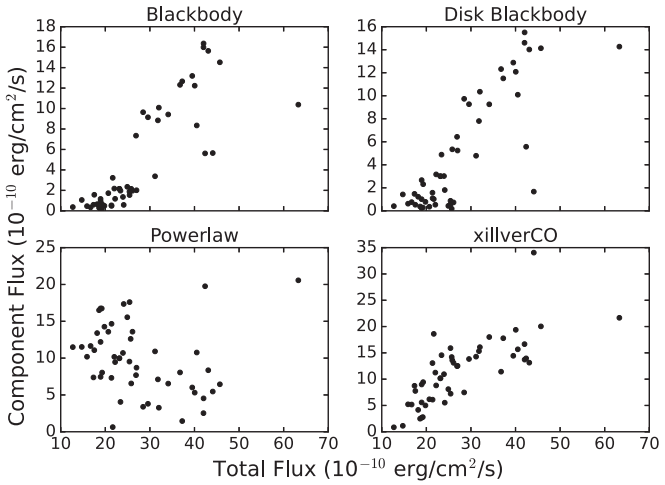

Figure 6. Shown are the fluxes of each component for each observation plotted against the overall flux of the system. In general, the component fluxes are well correlated with the overall flux (spearman rank $\geqslant$0.75), with the exception of the power-law flux, which is anticorrelated (spearman rank ~ -0.5).

We find in this analysis that the flux patterns persist over longer timescales as well. We show in Figure 6 that, in general, the flux of each component is increasing with overall flux except the power-law component. This is consistent with the well-documented low–hard and high–soft states, where higher flux observations are more thermally dominated and lower flux states are more dominated by nonthermal coronal emission. These correlations are supported by a Spearman rank $\geqslant$0.75 for all components except the anticorrelated power law, which is at a Spearman rank of ~ -0.5. We also note that the anticorrelation of the power-law flux and XILLVERCO flux discussed above is supported by a Spearman rank of -0.6.

The truncated inner disk at the low-flux state is pointed to as an analogy for BH-LMXB systems, which tend to show a larger value of $R_{\rm in}$ for low luminosities (which is correlated with the mass accretion rate, C. Done et al. 2007; J. A. Tomsick et al. 2009; J. A. García et al. 2015). However, over longer timescales, 4U 0614+091 does not appear to strongly show any correlation between inner disk radius and flux, aside from a slight preference for truncation in the lowest flux states. This relationship is shown in Figure 7, and even though the lowest flux states display some disk truncation, we see a random assortment of higher flux observations with equally or more truncated disks. We test a handful of lower flux observations to see if the disk truncation can be accounted for by the magnetic field. In some NS LMXBs, the magnetic field is able to truncate the disk at the Alfvén radius ($r_{\rm A}$), where the energy density of the magnetic field equals the energy density of the accreting material. To do this we calculate the strength of the equatorial magnetic field during our most truncated observation using the following equation from R. M. Ludlam et al. (2020):

$$B = 3.5 \times 10^5\, k_A^{-7/4} x^{7/4} \left(\frac{M}{1.4\ M_\odot}\right)^2 \left(\frac{10\ \mathrm{km}}{R_{\rm NS}}\right)^3 \times \left(\frac{f_{\rm ang}}{\eta}\frac{F_{\rm bol}}{10^{-9}\ \mathrm{erg\ s^{-1}cm^{-2}}}\right)^{1/2} \frac{D}{3.5\ \mathrm{kpc}}\ \mathrm{G} \quad (2)$$

where the efficiency η is assumed to be 0.2 (N. R. Sibgatullin & R. A. Sunyaev 2000), the conversion factor k_A and the angular anisotropy $f_{\rm ang}$ are set to unity (R. M. Ludlam et al. 2019), and

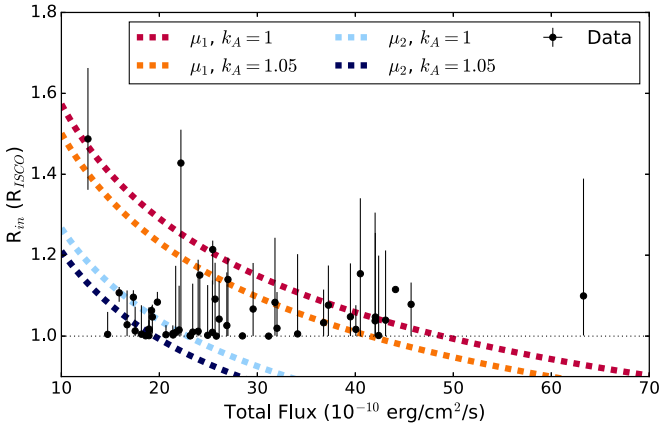

Figure 7. The overall flux of the system is poorly correlated with the inner disk radius. We see the lowest flux states display some degree of truncation, as stated in D. L. Moutard et al. (2023), but there are also higher flux states that are truncated just as heavily, if not more so. To test whether the observed disk truncation is caused by magnetic fields surrounding the NS, we plot the magnetosphere radius for various limits. Assuming our magnetic field upper limit (red dashed line) is well characterized by the lowest flux point does not yield a magnetosphere radius consistent with most measured $R_{\rm in}$ values. If instead we use a different low flux, seemingly truncated observation to characterize the magnetic field strength (blue dashed line), we find a slightly better relation, though it still cannot be concluded that the magnetic field is the sole source of inner disk truncation in this system. k_A, $f_{\rm ang}$, and η are all degenerate, so it is possible to make these magnetic field radii very small or very large, even using reasonable values for this parameter.

the distance D to 4U 0614+091 is 3.3 kpc (determined using GAIA data in R. M. Arnason et al. 2021). We use canonical NS values $M = 1.4\ M_\odot$ and $R_{\rm NS} = 10$ km, and the 0.5–50 keV flux and the inner disk radius (in R_g) are used for $F_{\rm bol}$ and x, respectively. If we use the lowest flux observation to determine our magnetic field strength, this provides an upper limit on the magnetic field of $B_1 \leqslant 0.4 \times 10^8$ G. We convert this value to a magnetic dipole moment (again assuming the values above) and find $\mu_1 = 3.8 \times 10^{25}\ \mathrm{G\,cm^{-3}}$. We use this value and mass accretion rate $\dot{m} = L/\eta c^2$ where L is the luminosity during that observation to calculate

$$r_A = \left(\frac{\mu^4}{GM\dot{m}^2}\right)^{1/7} \quad (3)$$

where G is the gravitational constant. This radius is plotted as a red dashed line in Figure 7. We see that this radius is generally too high to explain the inner disk radius in this case. These radii are generally too large to assume that the disk is truncating due to the magnetic field. If instead we use the next lowest flux observation with some indication of truncation to determine our magnetic field strength, we find $B_2 \leqslant 0.3 \times 10^8$G and $\mu_2 = 2.6 \times 10^{25}\ \mathrm{G\,cm^{-3}}$, for which we plot $r_{\rm A}$ as a blue dashed line in Figure 7.

If instead we assume $k_A = 0.5$ (M. Long et al. 2005), μ increases by roughly a factor of 3, which can drastically increase $r_{\rm A}$, especially in the case of μ_1. This would extend $r_{\rm A}$ beyond the truncated inner disk, meaning truncation cannot be caused by the magnetic field. If instead we assume $k_A = 1.05$ (below the theoretical upper limit of 1.1, discussed by A. Ibragimov & J. Poutanen 2009), we find that in some cases, the magnetosphere is consistently at or below the disk truncation. In such a case, it is possible that disk truncation is caused by the magnetic field during the low-flux states. We can see

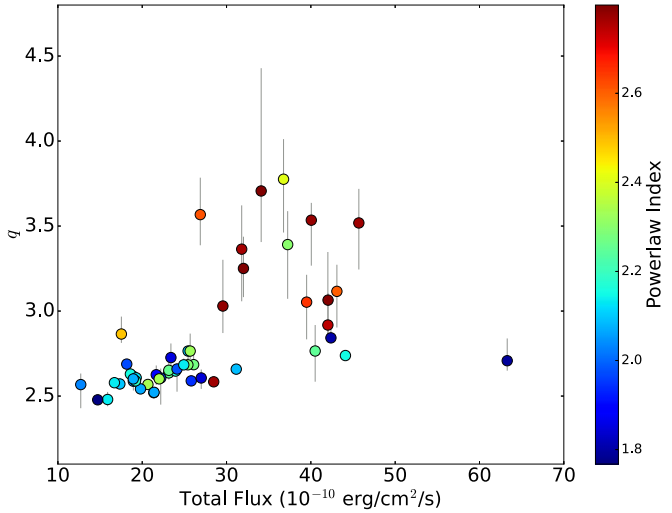

Figure 8. Shown is the emissivity index q plotted against the total unabsorbed flux of the system. Flatter emissivity profiles are generally consistent with the system in a low–hard state, while steeper values of q correspond with the high/soft state. This is potentially explained by a corona which is extending spatially during low-flux states.

similar changes to r_A by assuming different values of f_{ang}, (though it is expected to be near or above unity A. Ibragimov & J. Poutanen 2009) or η (which can vary depending on the rotational frequency of the NS). Because of this, we cannot confidently say that the low-flux disk truncation is caused exclusively by the magnetic field.

Another possibility for the cause of the disk truncation is disk depletion at low-mass accretion rates. However, this was explored for 4U 0614+091 in D. L. Moutard et al. (2023), which determined that the timescale required does not correspond with the cadence of observations. It should be noted that the degree of truncation is quite small, only extending up to $\sim 1.5\, R_{ISCO}$ (compare this to truncation up to $\sim 10\ R_{ISCO}$ as seen in Figure 5 of R. M. Ludlam 2024). This small degree of truncation, paired with the limitations of XILLVERCO at high flux (discussed in more detail in Section 4.3), makes drawing conclusions about the cause of the truncation difficult.

4.2. Emissivity Index

The emissivity index q is a value that represents the power-law index defining the illumination of the disk as a function of radius, r^{-q}. In the classical limit, $q = 3$, but this can be affected by multiple factors, such as the geometry of the illuminating corona and relativistic light bending (D. R. Wilkins 2018). One can use the emissivity index as a stand-in for how heavily light is curved toward the disk; in BH systems, this index is often much higher as the gravitational effects curve more of the emission to the regions of the disk closest to the BH. This leads to a steeper falloff in illumination near the inner disk ($q \gtrsim 6$ in the case of rapidly spinning BHs) before returning to the classical limit at the outer disk (D. R. Wilkins & A. C. Fabian 2012).

For NS systems, these values are typically closer to the classical limit. In this study we use only one emissivity index to minimize the number of free parameters, shown in Figure 8. By using only one value for q, we are essentially adopting an average value of the inner and outer emissivity indices. Values of $q < 3$, or a flattening of the emissivity index, may be indicative of a spatial extension of the illuminating corona. This may mean a vertical extension above the axis of the disk or a radial extension as the corona covers the inner region of the disk. We see in Figure 8 that for low-flux sources, q is generally consistent with a slightly flatter profile, while in higher flux states, the index tends to increase. This is also correlated with the spectral state of the system, as shown by the color bar representing the index of the power law. A larger power-law index is indicative of a softer spectrum, which is expected for higher flux states.

This relationship is potentially analogous to what is seen by E. Kara et al. (2019) for the BH transient system MAXI J1820+070. In that study, they propose a geometry wherein the corona extends vertically above the disk as the spectrum becomes harder. Similarly, D. J. K. Buisson et al. (2019) found a similar result for the same source, indicating that the height of the illuminating corona decreases as the spectrum softens. While NS and BH X-ray backgrounds (XRBs) are not exactly the same, the accretion processes are similar, so an analogy between these systems is not unreasonable. 4U 0614+091 is known to contain a relativistic jet during its hard states, though the jet alone is likely not a viable mechanism to produce hard X-rays and would also require some other source of Comptonized photons (S. Migliari et al. 2010). It is unlikely the jet is turning on and off on the timescale of weeks, following the quasiperiodic flux in the MAXI light curve. This provides evidence that the jet is not the driving source of the coronal photons, though it may contribute in some cases.

Another possible geometry of the spatially extended corona is one that expands radially rather than vertically above the disk. If at some point the disk becomes highly magnetized, this could provide the fields needed to produce the Comptonized corona, which would then illuminate the disk from directly above it. This too would lead to a flattening of the emissivity index over the region where the corona sits (D. R. Wilkins 2018). However, at least in active galactic nucleus systems, this coronal geometry is predicted primarily for high-flux states (D. R. Wilkins et al. 2014). In 4U 0614+091, the flattening of q appears to occur in the lower luminosity states, opposite to what is seen for systems where this geometry is well studied. Because of this, as well as the known existence of a jet for this source, we deem that geometry to be less likely. Therefore, the most likely scenario is a vertically extended corona. However, as mentioned in Section 4.1, the limitations of XILLVERCO make drawing broad conclusions about the transition into high–soft states difficult.

4.3. Limitations of XILLVERCO

It is worth noting that XILLVERCO assumes disk illumination by a nonthermal Comptonized component. This works well for UCXBs in the low–hard state but may begin to falter when faced with disks that are illuminated by thermal emission from near the NS itself. This regime is represented by the high–soft state, where we see q increase. This may serve to explain some of the discrepancies in the values of q for the few high flux but apparently soft points in Figure 8. These observations do not seem to agree with the overall trend of q increasing in the high-flux states. These outlier observations are also among those with the worst reduced χ^2 value. The self-consistent reflection model RELXILL also assumes illumination by a Comptonized corona, but the extension of the model, RELXILLNS, assumes thermal illumination. Similarly, a version of XILLVERCO with

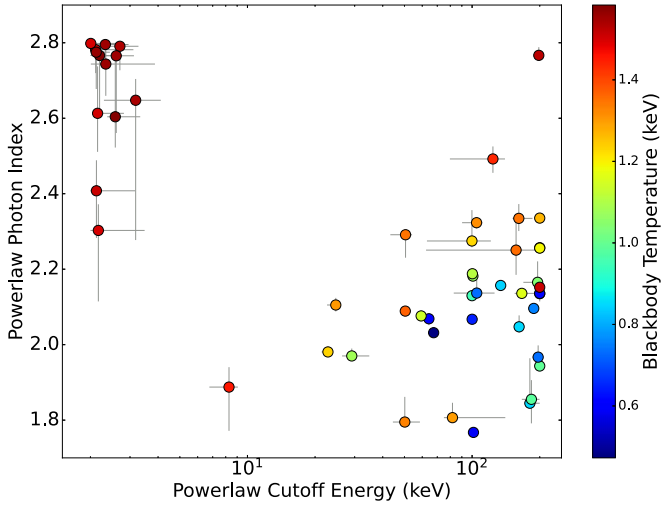

Figure 9. Shown here is the power-law photon index plotted against each spectrum's power-law cutoff energy, color coded by the blackbody temperature. While many observations demonstrate the expected behavior of a soft spectrum with a high blackbody temperature, some of the highest-temperature blackbodies are coincident with steep illuminating powerlaws with very low energy cutoffs. These observations are at the edge of the limits of XILLVERCO, which assumes illumination by a power law, even if the disk is being physically illuminated by the thermal NS boundary layer. In these cases, the model attempts to force the illuminating power law into a shape resembling that of a blackbody.

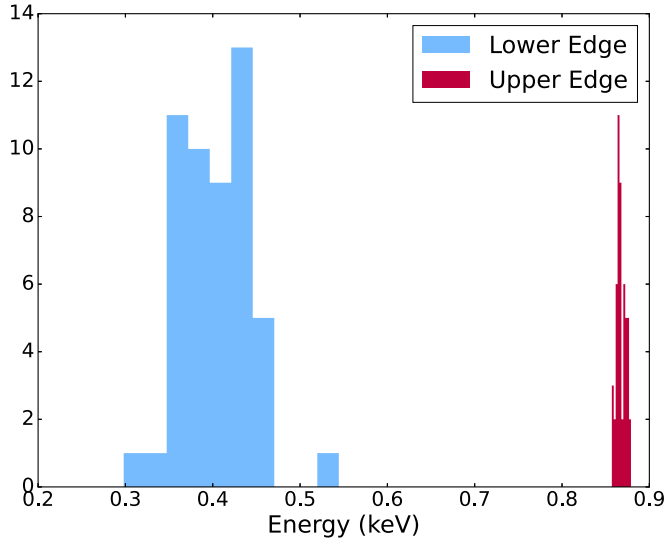

Figure 10. The distribution of edge energies for the model containing both edges. We see that the higher energy edge near 0.87 keV (consistent with an Ne K or Fe L edge) is very well constrained, while the lower energy edge around 0.4 keV (consistent with an N detector edge) has a significant amount of spread. This is to be expected for a feature that sits at or below the given NICER band but should be addressed more carefully in future studies with higher resolutions and improved collecting areas at the softest energies.

thermal illumination would be useful to describe the source in all states.

Figure 9 demonstrates one such limit of XILLVERCO. The bottom-right region of the plot shows the coolest blackbody temperatures being associated with shallow photon indices and high energy cutoffs, as expected for harder spectral states. As the blackbody temperature increases, we see either an increase in the power-law index or a decrease in the cutoff energy (the two parameters are somewhat degenerate, especially when the energy cutoff sits beyond the NICER band used in the study). However, in the top-left region of the plot, we see that the observations with the highest blackbody temperatures demonstrate a very soft power-law spectrum. These represent a regime where the illuminating power law shifts to the lowest energies and cuts off quite steeply. A steep, absorbed power law with a very low energy cutoff mimics the shape of a blackbody. Figure 1 in J. A. García et al. (2022) demonstrates the difference between XILLVER and XILLVERNS. We see therein that even when the incident spectrum mimics the shape of a blackbody illuminating the disk, the resulting reflection spectrum depends heavily on the input model used. For this study, that means that using a model with the incorrect input spectrum can cause some of the modeled parameters to tend toward unphysical values.

4.4. Absorption Edges

In the model we include two absorption edges in the lowest energies to account for apparent features at roughly 0.4 and 0.87 keV (corresponding roughly to an N detector edge and an Fe L or Ne K edge, respectively.) The inclusion of absorption edges surrounding the O VIII feature at ∼0.7 keV can cause some interference with the measurements of the feature itself. Between the two edges, the higher energy edge is much more well constrained, as shown in Figure 10. The lower edge is less constrained, but that is to be expected as it sits at or below the lower end of the NICER band in use. As a result, we initially test fits using only one edge centered near 0.87 keV, while keeping the rest of the model the same. The reduced χ^2 of the fits worsens marginally when the lower energy edge is removed. We find that the distributions of most parameters do not vary greatly, with some exceptions. $A_{\rm CO}$ tends to increase dramatically when one edge is removed, offering values up to 20 times higher than those from models with two edges. These carbon–oxygen abundances, reaching up to several hundred times Solar, are inconsistent with O. K. Madej et al. (2014) when accounting for the fact that the abundances in that paper are artificially increased in that version of the model. D. L. Moutard et al. (2023) finds the value of $A_{\rm CO}$ to be near 25, which is broadly consistent with O. K. Madej et al. (2014; though it should be noted that two edges are also used in D. L. Moutard et al. 2023).

We also find that the model with only one edge tends to fit the soft state using a harder power-law photon index than is physically reasonable for these states, although with a low energy cutoff. This model trends toward $\Gamma \leqslant 1.2$ during the softest states, which is only observed in the extreme hard states for NS systems (R. Ludlam et al. 2016; A. S. Parikh et al. 2017). While the trends between the models do not match, the conclusions drawn from Figure 9 remain: in the soft state, the power-law component cutoff energy shifts to imitate a thermal component. With only one edge, the trend seen in Figures 8 and 7 is also less consistent, with more spread in these parameters. We further test the validity of the edges by fixing their energies at 0.4016 keV and 0.8669 keV, corresponding to the laboratory values of the N edge and the Ne K edge. We choose the Ne K edge value over the Fe L edge as it is much closer to the average free value of 0.8677. Similarly to the test with one edge, while some outliers do appear, the overall distributions of parameters remain similar to the free energy fits. Again we see some increase in $A_{\rm CO}$, though not as dramatically as in our single-edge test. We also see some discrepancies in the disk blackbody temperature, which is

unsurprising as the central energy often coincides with the lower energy edge. However, other key parameters studied over the course of this paper, such as $R_{\rm in}$ and the emissivity index, maintain very similar values after freezing the edge energies. For completeness, we also test a handful of observations with no edges at all. When not accounting for the well-constrained higher energy edge, we found that the reduced χ^2 increases drastically for every observation checked, sometimes by a factor of greater than 5. Because of this, we do not pursue such a model further. Without a careful study of these absorption edges at low energy, it is difficult to say which model best explains the physical nature of the system. As a result we primarily focus on the model that is a more direct comparison with D. L. Moutard et al. (2023), but this does encourage a low-energy, high-resolution study of this source to better constrain the edge components.

5. Conclusion

In this study, we examine the long-term behavior of 4U 0614 +091 via 51 archival NICER spectra. These spectra cover a range of time spanning over 5 yr, and capture the source in various different spectral and flux states. After using XILLVERCO, a reflection model designed for UCXBs, we are able to say the following about this source:

1. The flux behavior is consistent with D. L. Moutard et al. (2023), which follows along the conventional high–soft and low–hard states. That is, as the overall unabsorbed flux of the system increases, so do the fluxes of most of the individual model components. The exception is the flux of the power law, which represents the Comptonized corona. This component decreases as the source gets brighter.
2. The relationship between the flux and $R_{\rm in}$ is seemingly uncorrelated but displays some agreement with D. L. Moutard et al. (2023), which finds that the lowest flux observations appear to show a truncated disk. This is true in some cases, but drawing any conclusion about the behavior of the inner disk is difficult with the given data.
3. The emissivity index tends to increase during the high–soft state when fit with XILLVERCO. This is indicative of the coronal extent increasing during harder states. A jet may exist during these states and could provide some contribution to the illumination of the disk from above the NS itself, but it is not likely the driving source. In softer states, the illuminating component may recede to be closer to the NS, causing the light to be curved more steeply toward the inner region of the disk. The picture of a corona extending further from the compact object as the spectrum hardens is also analogous to certain BH XRB systems.
4. The reflection model used here, XILLVERCO, may begin to falter in high-flux states, where disk illumination from a nonthermal corona gives way to thermal illumination from an NS boundary layer. In these cases, the model appears to shift the incident power law to the absolute lowest energies, mimicking the shape of a thermal illuminating component. During such states, the reflection model depends heavily on the correct illuminating component and therefore makes drawing conclusions about the source in the high-flux state difficult. This combined with a poor characterization of the lowest energy absorption edges leads to a model that is not complete when discussing UCXBs.

This long-term study of 4U 0614+091 paints a picture of a jetted UCXB that behaves similarly to other NS or BH LMXBs. The hard component appears to decrease in flux as the source gets brighter, and the inner disk truncation is poorly correlated with luminosity. The emissivity index provides a clue that a jet may contribute to the corona in hard states, while the illumination geometry shifts to be closer to the NS in softer states. Future high-resolution studies of reflection features with missions such as XRISM could help to better constrain the emissivity index and therefore the geometry of the illuminating component. This, paired with simultaneous radio measurements of the jet could also be enlightening to determine the extent of the jet's contribution to the corona as the spectrum changes between states. Polarimetry instruments such as IXPE can be used to probe coronal geometry in some systems and could potentially help to constrain our predictions of the extent of the corona in the soft states (H. Krawczynski et al. 2022). Also useful for this analysis would be a UCXB model, which accounts for disk illumination by the NS itself rather than a Comptonized corona.

Acknowledgments

This work is supported by NASA under grant No. 80NSSC22K0054. This research has made use of MAXI data provided by RIKEN, JAXA and the MAXI team (M. Matsuoka et al. 2009). This research has made use of data and/or software provided by the High Energy Astrophysics Science Archive Research Center (HEASARC), which is a service of the Astrophysics Science Division at NASA/GSFC. This research has made use of the NuSTAR Data Analysis Software (NuSTARDAS) jointly developed by the ASI Science Data Center (ASDC, Italy) and the California Institute of Technology (USA).

Appendix A
Observation Information

This section of the appendix summarizes all observations from NICER and NuSTAR used in this analysis. Table A1 displays the relevant observation information for each observation in the study.

Table A1
4U 0614+091 Observation Information

Observation ID	Obs. Start (UTC)	Exp. (ks)	Observation ID	Obs. Start (UTC)	Exp. (ks)
		NICER			
1050020115	2017-09-07 00:52:18	9.7	1050020225	2018-10-16 00:37:00	14.8
1050020116	2017-09-08 01:24:00	7.4	1050020226	2018-10-17 00:04:00	12.0
1050020117	2017-09-09 05:25:30	7.2	1050020229	2018-10-20 02:03:00	5.1
1050020118	2017-09-10 03:01:02	6.0	1050020230	2018-10-20 23:42:20	11.6
1050020119	2017-09-11 00:38:30	9.7	1050020232	2018-10-22 23:46:20	11.5
1050020121	2017-10-19 01:20:40	4.8	1050020236	2018-10-31 02:21:21	4.4
1050020123	2017-10-20 23:42:00	21.0	1050020241	2018-12-10 10:48:58	4.0
1050020124	2017-10-22 00:20:55	20.4	1050020242	2018-12-11 03:24:45	14.7
1050020125	2017-10-22 23:35:00	17.4	1050020243	2018-12-12 04:08:07	12.7
1050020126	2017-10-24 04:52:20	5.7	1050020244	2018-12-13 03:19:22	14.0
1050020127	2017-10-25 04:29:59	14.4	1050020252	2018-12-26 23:38:22	12.9
1050020128	2017-10-26 00:25:00	8.7	1050020255	2018-12-30 00:12:00	12.6
1050020146	2017-11-22 00:57:20	5.8	1050020256	2018-12-31 16:23:00	8.2
1050020182	2018-01-06 00:27:07	18.8	1050020257	2019-01-01 00:07:22	22.7
1050020183	2018-01-06 23:58:42	26.5	1050020269	2019-01-17 02:26:00	5.1
1050020184	2018-01-08 09:39:40	5.3	4701010101	2021-10-06 06:05:29	14.1
1050020185	2018-01-09 00:59:27	10.2	4701010201	2021-10-09 08:06:17	17.3
1050020186	2018-01-10 00:09:00	10.2	4701010301	2021-10-11 17:27:39	6.8
1050020187	2018-01-11 00:51:00	10.2	4701010302	2021-10-11 23:35:00	11.8
1050020188	2018-01-12 00:01:37	9.9	4701010401	2022-01-19 07:07:18	10.3
1050020198	2018-01-30 00:40:14	5.8	5050020204	2022-10-07 23:51:20	5.7
1050020213	2018-03-14 23:33:11	9.5	5050020206	2022-10-10 03:03:20	6.9
1050020214	2018-03-16 00:15:52	6.8	5050020208	2022-10-11 23:55:20	9.2
1050020218	2018-05-03 23:30:15	9.4	5050020221	2022-11-24 00:49:20	6.1
1050020222	2018-10-13 01:41:00	6.4	5050020222	2022-11-24 23:56:20	8.1
1050020224	2018-10-14 23:55:00	8.2			
		NuSTAR			
30363002002	2017-12-01 15:56:09	19.9	30702009002	2021-10-06 05:36:09	28.7
30702009004	2021-10-09 09:16:09	29.4	30702009006	2021-10-11 17:41:09	29.0
30702009008	2021-10-13 17:56:09	28.6	30702009010	2022-01-19 06:51:09	28.2

Appendix B
NICER Fit Parameters

This section of the appendix summarizes all of the final fit parameters used in both the initial continuum model as well as the reflection model for NICER. Table B1 displays the fit parameters for a continuum-only model. Table B2 displays the continuum parameters for a full reflection model, while Table B3 contains the reflection parameters. Table B4 contains the calculated fluxes for each component, as well as the equivalent width and central energy of the oxygen feature.

Table B1
4U 0614+091 Results of Continuum Modeling

OBSID	TBABS	EDGE 1		EDGE 2		BBODY		DISKBB		CUTOFFPL			
	N_H (10^{22} cm^{-2})	E (keV)	τ_{max}	E (keV)	τ_{max}	kT (keV)	k_{BB} (10^{-3})	kT (keV)	k_{DBB}	Γ	E_{cutoff} (keV)	k_{PL}	χ^2 (dof)
1050020115	$0.46^{+0.01}_{-0.02}$	$0.434^{+0.001}_{-0.002}$	2.6 ± 0.1	$0.847^{+0.003}_{-0.001}$	$0.296^{+0.01}_{-0.004}$	$1.44^{+0.013}_{-0.005}$	$16.02^{+0.03}_{-0.07}$	$0.571^{+0.007}_{-0.003}$	$1023.5^{+21.4}_{-62.5}$	$3.99^{+0.01}_{-0.04}$	$0.48^{+0.04}_{-0.01}$	$3.2^{+0.1}_{-0.5}$	1333(143)
1050020116	$0.12^{+0.02}_{-0.01}$	0.451 ± 0.001	2.7 ± 0.1	$0.858^{+0.002}_{-0.001}$	$0.399^{+0.007}_{-0.004}$	$1.54^{+0.03}_{-0.01}$	$12.6^{+1.1}_{-0.8}$	0.62 ± 0.01	$432.8^{+16.2}_{-33.4}$	2.2 ± 0.1	$483.1^{+16.9}_{-108.7}$	$0.28^{+0.03}_{-0.02}$	1308(131)
1050020117	$0.17^{+0.03}_{-0.02}$	$0.447^{+0.002}_{-0.001}$	$2.9^{+0.1}_{-0.2}$	$0.859^{+0.002}_{-0.001}$	0.43 ± 0.01	1.44 ± 0.02	$6.0^{+0.2}_{-0.7}$	$0.59^{+0.01}_{-0.02}$	$254.3^{+23.4}_{-27.5}$	$2.8^{+0.1}_{-0.2}$	$455.0^{+44.9}_{-98.0}$	$0.36^{+0.03}_{-0.01}$	1142(127)
1050020118	$0.15^{+0.02}_{-0.04}$	0.448 ± 0.001	2.9 ± 0.2	0.857 ± 0.001	0.43 ± 0.01	$1.46^{+0.03}_{-0.05}$	$4.0^{+0.3}_{-0.7}$	$0.57^{+0.02}_{-0.05}$	$160.6^{+44.3}_{-21.8}$	2.6 ± 0.1	$459.5^{+40.4}_{-230.0}$	0.38 ± 0.02	1021(124)
1050020119	$0.27^{+0.02}_{-0.01}$	0.445 ± 0.001	$3.0^{+0.1}_{-0.2}$	$0.858^{+0.002}_{-0.001}$	$0.379^{+0.004}_{-0.006}$	1.43 ± 0.01	$11.54^{+0.05}_{-0.06}$	$0.592^{+0.006}_{-0.003}$	$605.0^{+10.4}_{-36.2}$	$3.996^{+0.004}_{-0.032}$	$1.8^{+0.4}_{-0.1}$	$0.5^{+0.03}_{-0.04}$	1574(132)
1050020121	$0.15^{+0.03}_{-0.02}$	$0.449^{+0.002}_{-0.001}$	$2.9^{+0.2}_{-0.3}$	$0.858^{+0.001}_{-0.002}$	0.43 ± 0.01	$1.49^{+0.04}_{-0.02}$	$4.7^{+0.2}_{-0.9}$	0.57 ± 0.02	$177.9^{+11.8}_{-38.9}$	$2.63^{+0.04}_{-0.08}$	$435.5^{+64.1}_{-135.8}$	$0.42^{+0.04}_{-0.01}$	850(127)
1050020123	$0.193^{+0.004}_{-0.005}$	0.438 ± 0.001	$1.9^{+0.06}_{-0.04}$	$0.8577^{+0.0012}_{-0.0004}$	$0.397^{+0.005}_{-0.004}$	$0.01^{+0.02}_{-0.01}$	$0.02^{+0.03}_{-0.02}$	$0.214^{+0.002}_{-0.004}$	$4991.9^{+8.0}_{-44.7}$	$2.06^{+0.03}_{-0.01}$	$35.2^{+11.3}_{-3.2}$	$0.333^{+0.002}_{-0.001}$	3819(138)
1050020124	0.208 ± 0.004	0.436 ± 0.001	$2.14^{+0.03}_{-0.04}$	$0.857^{+0.0004}_{-0.0008}$	0.417 ± 0.004	1.45 ± 0.03	1.3 ± 0.1	$0.2002^{+0.0012}_{-0.0002}$	$4995.7^{+4.3}_{-107.6}$	2.35 ± 0.01	$490.6^{+9.4}_{-22.6}$	$0.41^{+0.002}_{-0.003}$	4137(138)
1050020125	$0.347^{+0.01}_{-0.004}$	0.441 ± 0.001	$2.33^{+0.02}_{-0.09}$	0.853 ± 0.001	$0.389^{+0.006}_{-0.001}$	$1.459^{+0.013}_{-0.004}$	$8.59^{+0.01}_{-0.06}$	$0.622^{+0.006}_{-0.002}$	$324.2^{+2.6}_{-16.7}$	$3.996^{+0.004}_{-0.014}$	$17.3^{+13.2}_{-1.6}$	0.49 ± 0.01	3522(138)
1050020126	$0.21^{+0.01}_{-0.02}$	0.451 ± 0.001	2.3 ± 0.1	$0.8552^{+0.0018}_{-0.0004}$	0.42 ± 0.01	$1.48^{+0.01}_{-0.03}$	$4.6^{+0.3}_{-0.6}$	$0.55^{+0.01}_{-0.02}$	$208.7^{+37.2}_{-18.4}$	$2.61^{+0.04}_{-0.05}$	$463.7^{+36.3}_{-109.0}$	0.53 ± 0.02	1426(129)
1050020127	0.201 ± 0.005	0.438 ± 0.001	2.09 ± 0.05	0.857 ± 0.001	$0.417^{+0.005}_{-0.006}$	$1.37^{+0.08}_{-0.03}$	0.7 ± 0.2	$0.211^{+0.004}_{-0.006}$	$4980.6^{+19.4}_{-97.1}$	$2.26^{+0.03}_{-0.02}$	$412.1^{+87.3}_{-93.2}$	$0.386^{+0.007}_{-0.004}$	3052(136)
1050020128	0.12 ± 0.01	0.451 ± 0.001	$2.5^{+0.1}_{-0.2}$	$0.854^{+0.002}_{-0.001}$	0.4 ± 0.01	$0.63^{+0.02}_{-0.04}$	0.6 ± 0.1	$0.211^{+0.009}_{-0.004}$	$4969.5^{+30.2}_{-176.3}$	$2.1^{+0.01}_{-0.02}$	$454.7^{+44.9}_{-217.5}$	0.3 ± 0.01	1368(131)
1050020146	0.32 ± 0.02	0.445 ± 0.001	2.6 ± 0.1	$0.856^{+0.001}_{-0.002}$	$0.34^{+0.009}_{-0.003}$	$1.51^{+0.02}_{-0.01}$	19.9 ± 0.1	$0.645^{+0.008}_{-0.002}$	$589.0^{+8.5}_{-37.1}$	$3.998^{+0.002}_{-0.022}$	$1.7^{+0.3}_{-0.1}$	$0.62^{+0.03}_{-0.06}$	1165(136)
1050020182	0.47 ± 0.01	0.44 ± 0.001	2.5 ± 0.1	0.847 ± 0.001	$0.298^{+0.006}_{-0.003}$	$1.373^{+0.007}_{-0.002}$	$13.27^{+0.02}_{-0.05}$	$0.5397^{+0.0035}_{-0.0004}$	$1179.3^{+1.2}_{-40.2}$	$3.9999^{+0.0001}_{-0.0129}$	$0.443^{+0.013}_{-0.003}$	$3.8^{+0.1}_{-0.3}$	3060(141)
1050020183	$0.488^{+0.001}_{-0.009}$	$0.4321^{+0.0001}_{-0.001}$	$2.48^{+0.05}_{-0.02}$	$0.8456^{+0.0014}_{-0.0002}$	$0.299^{+0.002}_{-0.005}$	$1.381^{+0.004}_{-0.005}$	$13.86^{+0.02}_{-0.04}$	$0.545^{+0.002}_{-0.001}$	$1176.7^{+7.2}_{-27.4}$	3.99 ± 0.01	$0.446^{+0.01}_{-0.003}$	$3.97^{+0.01}_{-0.23}$	4266(149)
1050020184	$0.18^{+0.01}_{-0.02}$	$0.454^{+0.001}_{-0.002}$	$2.3^{+0.2}_{-0.1}$	$0.859^{+0.002}_{-0.001}$	0.41 ± 0.01	$0.349^{+0.007}_{-0.005}$	$2.8^{+0.1}_{-0.2}$	$0.201^{+0.012}_{-0.001}$	$3686.0^{+263.7}_{-2748.5}$	$2.11^{+0.02}_{-0.01}$	$327.0^{+171.4}_{-120.4}$	0.57 ± 0.01	1515(132)
1050020185	$0.221^{+0.004}_{-0.009}$	$0.446^{+0.001}_{-0.002}$	$2.07^{+0.08}_{-0.03}$	0.857 ± 0.001	$0.429^{+0.003}_{-0.008}$	$1.61^{+0.08}_{-0.03}$	$1.3^{+0.2}_{-0.1}$	$0.2003^{+0.0021}_{-0.0003}$	$4670.1^{+266.8}_{-1311.6}$	$2.43^{+0.03}_{-0.02}$	$339.3^{+160.7}_{-72.5}$	$0.418^{+0.007}_{-0.004}$	1822(133)
1050020186	0.16 ± 0.01	0.454 ± 0.001	2.0 ± 0.1	$0.854^{+0.001}_{-0.002}$	0.39 ± 0.01	$0.56^{+0.03}_{-0.01}$	$0.62^{+0.04}_{-0.1}$	$0.208^{+0.001}_{-0.006}$	$4923.2^{+76.7}_{-316.6}$	$2.115^{+0.03}_{-0.002}$	$344.5^{+155.2}_{-34.6}$	$0.241^{+0.01}_{-0.002}$	1131(130)
1050020187	0.35 ± 0.01	0.44 ± 0.001	2.2 ± 0.1	0.856 ± 0.001	$0.389^{+0.006}_{-0.004}$	1.46 ± 0.01	$7.33^{+0.03}_{-0.07}$	0.63 ± 0.01	$270.2^{+10.6}_{-16.7}$	$3.999^{+0.001}_{-0.034}$	$26.3^{+26.4}_{-5.8}$	$0.44^{+0.01}_{-0.02}$	1890(135)
1050020188	0.35 ± 0.01	$0.438^{+0.001}_{-0.002}$	2.3 ± 0.1	0.856 ± 0.001	$0.377^{+0.005}_{-0.004}$	$1.45^{+0.02}_{-0.01}$	$8.77^{+0.03}_{-0.09}$	$0.607^{+0.007}_{-0.003}$	$393.9^{+4.4}_{-29.1}$	$3.998^{+0.002}_{-0.016}$	$5.5^{+2.8}_{-0.3}$	$0.49^{+0.01}_{-0.03}$	1790(136)
1050020198	$0.21^{+0.01}_{-0.02}$	0.451 ± 0.001	2.4 ± 0.1	$0.86^{+0.001}_{-0.002}$	0.41 ± 0.01	1.52 ± 0.03	$4.4^{+0.4}_{-0.8}$	$0.6^{+0.02}_{-0.03}$	$115.4^{+18.3}_{-17.8}$	$2.67^{+0.05}_{-0.1}$	$482.9^{+17.0}_{-219.3}$	$0.48^{+0.02}_{-0.01}$	1124(129)
1050020213	0.44 ± 0.01	$0.439^{+0.001}_{-0.002}$	$2.52^{+0.05}_{-0.11}$	$0.85^{+0.002}_{-0.001}$	$0.295^{+0.008}_{-0.003}$	1.49 ± 0.01	$18.6^{+0.01}_{-0.11}$	$0.597^{+0.006}_{-0.001}$	$895.2^{+2.5}_{-37.6}$	$3.999^{+0.001}_{-0.02}$	$0.545^{+0.026}_{-0.002}$	$2.53^{+0.04}_{-0.2}$	1543(139)
1050020214	$0.36^{+0.01}_{-0.02}$	$0.439^{+0.002}_{-0.001}$	2.3 ± 0.1	$0.8546^{+0.0024}_{-0.0003}$	$0.342^{+0.005}_{-0.004}$	1.56 ± 0.01	19.4 ± 0.1	$0.655^{+0.006}_{-0.004}$	$544.8^{+15.0}_{-19.2}$	$3.998^{+0.002}_{-0.021}$	$2.7^{+0.7}_{-0.2}$	$0.59^{+0.01}_{-0.06}$	1304(137)
1050020218	0.32 ± 0.01	$0.428^{+0.002}_{-0.001}$	2.7 ± 0.1	0.857 ± 0.001	0.39 ± 0.01	1.41 ± 0.01	$8.95^{+0.02}_{-0.08}$	$0.59^{+0.006}_{-0.003}$	$455.3^{+11.5}_{-26.3}$	$3.996^{+0.004}_{-0.026}$	$3.3^{+1.3}_{-0.4}$	$0.44^{+0.02}_{-0.03}$	1271(124)
1050020222	0.2 ± 0.02	0.45 ± 0.001	2.5 ± 0.1	0.858 ± 0.001	0.42 ± 0.01	$1.51^{+0.02}_{-0.03}$	$5.2^{+0.4}_{-0.7}$	$0.58^{+0.01}_{-0.03}$	$195.9^{+30.3}_{-18.2}$	2.7 ± 0.1	$472.9^{+27.1}_{-71.6}$	$0.42^{+0.02}_{-0.01}$	1267(128)
1050020224	0.17 ± 0.01	0.451 ± 0.001	2.4 ± 0.1	$0.857^{+0.002}_{-0.001}$	0.43 ± 0.01	1.6 ± 0.1	0.8 ± 0.2	$0.2002^{+0.0028}_{-0.0002}$	$4833.0^{+166.7}_{-1023.3}$	$2.35^{+0.02}_{-0.03}$	$404.8^{+95.0}_{-174.7}$	$0.371^{+0.003}_{-0.006}$	1346(128)
1050020225	$0.175^{+0.006}_{-0.005}$	0.444 ± 0.001	$2.19^{+0.04}_{-0.06}$	0.856 ± 0.001	0.41 ± 0.01	$0.7^{+0.2}_{-0.1}$	0.12 ± 0.02	0.203 ± 0.003	$4979.0^{+21.0}_{-141.4}$	2.21 ± 0.01	$394.7^{+104.6}_{-136.5}$	$0.31^{+0.003}_{-0.004}$	2136(134)
1050020226	0.33 ± 0.01	$0.4381^{+0.0018}_{-0.0004}$	$2.53^{+0.03}_{-0.11}$	0.855 ± 0.001	$0.371^{+0.008}_{-0.001}$	1.43 ± 0.01	$9.52^{+0.06}_{-0.03}$	0.597 ± 0.004	$463.9^{+12.5}_{-18.3}$	$3.999^{+0.001}_{-0.015}$	$3.4^{+0.9}_{-0.1}$	$0.49^{+0.01}_{-0.03}$	2215(136)
1050020229	$0.33^{+0.01}_{-0.02}$	0.444 ± 0.002	2.5 ± 0.1	$0.856^{+0.001}_{-0.002}$	$0.343^{+0.008}_{-0.004}$	1.47 ± 0.01	$16.6^{+0.04}_{-0.12}$	$0.622^{+0.006}_{-0.003}$	$681.8^{+12.9}_{-36.6}$	$3.97^{+0.03}_{-0.002}$	$1.49^{+0.32}_{-0.05}$	$0.69^{+0.03}_{-0.09}$	1016(134)
1050020230	0.35 ± 0.01	0.44 ± 0.001	2.4 ± 0.1	0.854 ± 0.001	$0.382^{+0.004}_{-0.006}$	1.46 ± 0.01	$8.86^{+0.04}_{-0.08}$	$0.622^{+0.007}_{-0.004}$	$343.8^{+7.4}_{-21.0}$	$3.99^{+0.01}_{-0.02}$	$5.0^{+2.3}_{-0.2}$	$0.5^{+0.01}_{-0.02}$	2152(137)
1050020232	$0.179^{+0.01}_{-0.005}$	0.445 ± 0.001	$2.11^{+0.05}_{-0.11}$	0.857 ± 0.001	$0.407^{+0.005}_{-0.007}$	0.7 ± 0.1	$0.29^{+0.08}_{-0.03}$	$0.21^{+0.007}_{-0.003}$	$4995.4^{+4.6}_{-147.5}$	$2.2^{+0.02}_{-0.01}$	$472.7^{+27.2}_{-211.4}$	$0.303^{+0.005}_{-0.007}$	1625(133)
1050020236	$0.27^{+0.01}_{-0.03}$	$0.447^{+0.001}_{-0.002}$	$2.9^{+0.2}_{-0.1}$	0.857 ± 0.002	$0.356^{+0.003}_{-0.01}$	$1.51^{+0.02}_{-0.01}$	16.8 ± 0.1	$0.629^{+0.008}_{-0.003}$	$636.0^{+8.9}_{-38.9}$	$3.99^{+0.01}_{-0.04}$	$1.9^{+0.5}_{-0.2}$	$0.52^{+0.02}_{-0.08}$	959(133)
1050020241	$0.13^{+0.03}_{-0.01}$	$0.45^{+0.002}_{-0.001}$	$2.9^{+0.1}_{-0.2}$	$0.859^{+0.002}_{-0.001}$	0.41 ± 0.01	1.6 ± 0.1	$2.6^{+0.3}_{-0.5}$	$0.52^{+0.04}_{-0.05}$	$97.5^{+30.0}_{-33.9}$	$2.42^{+0.03}_{-0.04}$	$409.7^{+90.2}_{-177.5}$	$0.49^{+0.04}_{-0.02}$	860(126)
1050020242	$0.198^{+0.007}_{-0.002}$	0.439 ± 0.001	$1.85^{+0.03}_{-0.07}$	0.858 ± 0.001	$0.39^{+0.006}_{-0.004}$	$0.65^{+0.04}_{-0.02}$	$0.51^{+0.05}_{-0.1}$	$0.222^{+0.003}_{-0.004}$	$4993.5^{+6.5}_{-68.5}$	$2.1^{+0.02}_{-0.01}$	$465.8^{+33.7}_{-164.0}$	$0.329^{+0.009}_{-0.003}$	2660(137)
1050020243	$0.173^{+0.005}_{-0.008}$	0.447 ± 0.001	2.0 ± 0.1	0.856 ± 0.001	$0.392^{+0.007}_{-0.004}$	0.64 ± 0.02	0.8 ± 0.1	$0.222^{+0.006}_{-0.004}$	$4980.6^{+19.4}_{-77.8}$	$2.07^{+0.01}_{-0.02}$	$492.3^{+7.7}_{-253.2}$	0.29 ± 0.01	1989(136)
1050020244	$0.348^{+0.001}_{-0.014}$	$0.4339^{+0.0016}_{-0.0001}$	$2.0^{+0.09}_{-0.02}$	$0.8538^{+0.0014}_{-0.0004}$	$0.401^{+0.007}_{-0.003}$	$1.67^{+0.03}_{-0.01}$	6.8 ± 0.1	$0.81^{+0.02}_{-0.01}$	$68.9^{+1.8}_{-6.6}$	$3.57^{+0.02}_{-0.07}$	$496.0^{+4.0}_{-73.3}$	0.5 ± 0.01	2604(137)
1050020252	0.44 ± 0.01	0.44 ± 0.001	$2.55^{+0.04}_{-0.09}$	0.849 ± 0.001	$0.284^{+0.006}_{-0.002}$	$1.503^{+0.004}_{-0.007}$	$27.66^{+0.03}_{-0.11}$	$0.607^{+0.004}_{-0.001}$	$1149.4^{+10.4}_{-33.2}$	$3.998^{+0.002}_{-0.025}$	$0.52^{+0.02}_{-0.01}$	$3.5^{+0.1}_{-0.3}$	2526(144)
1050020255	0.49 ± 0.01	0.432 ± 0.001	$2.46^{+0.03}_{-0.08}$	0.846 ± 0.001	$0.283^{+0.007}_{-0.001}$	1.44 ± 0.01	$19.17^{+0.03}_{-0.07}$	$0.567^{+0.003}_{-0.002}$	$1343.3^{+19.7}_{-39.0}$	3.99 ± 0.01	$0.462^{+0.019}_{-0.002}$	$4.6^{+0.1}_{-0.4}$	2429(140)
1050020256	0.36 ± 0.01	0.441 ± 0.001	2.3 ± 0.1	0.854 ± 0.001	0.367 ± 0.004	1.45 ± 0.01	$12.11^{+0.04}_{-0.08}$	$0.6^{+0.005}_{-0.004}$	$599.6^{+20.4}_{-24.3}$	$3.998^{+0.002}_{-0.018}$	$4.1^{+1.6}_{-0.1}$	$0.63^{+0.01}_{-0.04}$	1955(137)
1050020257	$0.496^{+0.004}_{-0.006}$	0.432 ± 0.001	$2.42^{+0.03}_{-0.05}$	0.847 ± 0.001	$0.287^{+0.006}_{-0.001}$	1.409 ± 0.004	$16.16^{+0.03}_{-0.05}$	$0.546^{+0.002}_{-0.001}$	$1398.4^{+11.6}_{-25.5}$	$3.9997^{+0.0003}_{-0.0178}$	$0.446^{+0.01}_{-0.003}$	$4.8^{+0.1}_{-0.2}$	4455(149)
1050020269	$0.33^{+0.02}_{-0.01}$	$0.445^{+0.001}_{-0.003}$	2.5 ± 0.1	$0.857^{+0.002}_{-0.001}$	$0.359^{+0.008}_{-0.004}$	1.47 ± 0.01	11.4 ± 0.1	$0.606^{+0.006}_{-0.004}$	$533.9^{+15.8}_{-29.2}$	$3.99^{+0.01}_{-0.03}$	$2.4^{+0.6}_{-0.2}$	$0.6^{+0.03}_{-0.04}$	1018(131)
4701010101	$0.333^{+0.004}_{-0.024}$	$0.438^{+0.002}_{-0.001}$	$2.35^{+0.03}_{-0.09}$	0.854 ± 0.001	$0.394^{+0.013}_{-0.001}$	1.48 ± 0.02	$6.79^{+0.04}_{-0.2}$	$0.614^{+0.012}_{-0.005}$	$252.8^{+8.5}_{-40.0}$	$3.97^{+0.02}_{-0.24}$	$482.9^{+16.8}_{-52.8}$	0.38 ± 0.01	2282(133)

Table B1
(Continued)

OBSID	TBABS	EDGE 1		EDGE 2		BBODY		DISKBB		CUTOFFPL			χ^2
	$N_{\rm H}$ (10^{22} cm^{-2})	E (keV)	$\tau_{\rm max}$	E (keV)	$\tau_{\rm max}$	kT (keV)	$k_{\rm BB}$ (10^{-3})	kT (keV)	$k_{\rm DBB}$	Γ	$E_{\rm cutoff}$ (keV)	$k_{\rm PL}$	(dof)
4701010201	0.34 ± 0.01	0.431 ± 0.001	$2.39^{+0.02}_{-0.08}$	0.855 ± 0.001	$0.391^{+0.005}_{-0.004}$	$1.528^{+0.03}_{-0.002}$	$5.49^{+0.04}_{-0.05}$	$0.69^{+0.012}_{-0.002}$	$118.6^{+1.5}_{-10.1}$	$3.98^{+0.02}_{-0.07}$	$398.3^{+98.0}_{-179.4}$	$0.355^{+0.008}_{-0.003}$	2616(134)
4701010301	$0.18^{+0.02}_{-0.03}$	0.458 ± 0.003	1.5 ± 0.2	$0.845^{+0.004}_{-0.003}$	0.29 ± 0.01	0.48 ± 0.01	0.9 ± 0.2	$0.201^{+0.009}_{-0.001}$	$2529.8^{+1434.0}_{-1885.2}$	$2.02^{+0.03}_{-0.04}$	$468.0^{+31.8}_{-256.6}$	0.18 ± 0.01	338(123)
4701010302	$0.21^{+0.01}_{-0.02}$	$0.458^{+0.001}_{-0.002}$	1.4 ± 0.1	$0.842^{+0.003}_{-0.001}$	$0.3^{+0.008}_{-0.003}$	0.47 ± 0.01	$1.0^{+0.02}_{-0.09}$	$0.2001^{+0.0034}_{-0.0001}$	$4902.0^{+98.0}_{-968.2}$	$1.98^{+0.02}_{-0.01}$	$498.3^{+1.7}_{-23.1}$	$0.178^{+0.006}_{-0.002}$	725(130)
4701010401	$0.209^{+0.01}_{-0.005}$	0.445 ± 0.001	1.9 ± 0.1	0.856 ± 0.001	$0.399^{+0.007}_{-0.004}$	1.9 ± 0.1	$1.09^{+0.15}_{-0.05}$	$0.2003^{+0.0014}_{-0.0003}$	$4961.7^{+38.3}_{-156.3}$	$2.28^{+0.02}_{-0.01}$	$491.2^{+8.8}_{-73.3}$	$0.401^{+0.004}_{-0.002}$	1764(133)
5050020204	0.12 ± 0.02	$0.448^{+0.002}_{-0.001}$	2.9 ± 0.2	$0.861^{+0.001}_{-0.002}$	0.42 ± 0.01	$1.47^{+0.03}_{-0.04}$	$2.9^{+0.4}_{-0.5}$	0.51 ± 0.02	$181.8^{+32.9}_{-25.4}$	2.5 ± 0.1	$378.3^{+120.7}_{-178.2}$	0.34 ± 0.02	964(125)
5050020206	$0.28^{+0.01}_{-0.02}$	0.444 ± 0.002	2.4 ± 0.1	$0.857^{+0.002}_{-0.001}$	0.35 ± 0.01	1.52 ± 0.01	19.8 ± 0.1	0.63 ± 0.004	$647.3^{+17.2}_{-19.5}$	$3.99^{+0.01}_{-0.03}$	$7.7^{+6.6}_{-1.4}$	$0.34^{+0.01}_{-0.04}$	1473(135)
5050020208	$0.23^{+0.01}_{-0.02}$	0.443 ± 0.001	2.1 ± 0.1	0.859 ± 0.001	$0.405^{+0.009}_{-0.002}$	$1.45^{+0.02}_{-0.01}$	$7.0^{+0.1}_{-1.1}$	$0.55^{+0.01}_{-0.02}$	$386.0^{+24.8}_{-34.9}$	$2.85^{+0.01}_{-0.19}$	$321.2^{+178.3}_{-142.6}$	$0.38^{+0.03}_{-0.01}$	2206(134)
5050020221	$0.3^{+0.01}_{-0.02}$	$0.444^{+0.002}_{-0.001}$	2.5 ± 0.1	$0.858^{+0.001}_{-0.002}$	$0.356^{+0.008}_{-0.004}$	1.47 ± 0.01	16.0 ± 0.1	$0.597^{+0.005}_{-0.003}$	$780.0^{+21.8}_{-33.3}$	$3.99^{+0.01}_{-0.02}$	$1.5^{+0.4}_{-0.1}$	$0.53^{+0.02}_{-0.09}$	1568(135)
5050020222	0.19 ± 0.01	0.449 ± 0.001	2.3 ± 0.1	$0.858^{+0.002}_{-0.001}$	$0.415^{+0.004}_{-0.005}$	$1.62^{+0.04}_{-0.03}$	2.5 ± 0.3	$0.53^{+0.03}_{-0.06}$	$58.8^{+26.1}_{-7.8}$	$2.54^{+0.03}_{-0.05}$	$475.9^{+24.0}_{-224.0}$	0.42 ± 0.01	1416(130)

Table B2
4U 0614+091 Results of Reflection Modeling: Continuum Parameters

OBSID	TBABS	EDGE 1		EDGE 2		BBODY		DISKBB		CUTOFFPL		
	$N_{\rm H}$ (10^{22} cm^{-2})	E (keV)	$\tau_{\rm max}$	E (keV)	$\tau_{\rm max}$	kT (keV)	$k_{\rm BB}$ (10^{-3})	kT (keV)	$k_{\rm DBB}$	Γ	$E_{\rm cutoff}$ (keV)	$k_{\rm PL}$
1050020115	$0.48^{+0.01}_{-0.02}$	$0.444^{+0.002}_{-0.003}$	1.3 ± 0.1	0.87 ± 0.01	$0.12^{+0.02}_{-0.01}$	$1.512^{+0.019}_{-0.004}$	$15.0^{+0.1}_{-0.5}$	$0.642^{+0.004}_{-0.01}$	$435.4^{+16.2}_{-34.8}$	2.4 ± 0.1	$2.13^{+1.04}_{-0.13}$	$0.44^{+0.03}_{-0.11}$
1050020116	$0.307^{+0.005}_{-0.004}$	$0.457^{+0.005}_{-0.001}$	$0.736^{+0.004}_{-0.084}$	$0.879^{+0.0041}_{-0.0005}$	$0.214^{+0.001}_{-0.003}$	$1.3^{+0.02}_{-0.01}$	$6.7^{+0.1}_{-0.3}$	$0.531^{+0.002}_{-0.036}$	$487.2^{+64.6}_{-79.9}$	$1.81^{+0.04}_{-0.01}$	$81.8^{+58.8}_{-6.9}$	$0.22^{+0.01}_{-0.05}$
1050020117	$0.37^{+0.004}_{-0.005}$	0.37 ± 0.01	$1.19^{+0.02}_{-0.05}$	0.868 ± 0.003	0.217 ± 0.003	1.2 ± 0.02	2.57 ± 0.02	$0.415^{+0.004}_{-0.002}$	$696.7^{+15.2}_{-25.5}$	$2.257^{+0.004}_{-0.008}$	$200.0^{\dagger}$	$0.2^{+0.001}_{-0.002}$
1050020118	$0.367^{+0.003}_{-0.001}$	$0.364^{+0.004}_{-0.008}$	$0.628^{+0.014}_{-0.005}$	$0.865^{+0.003}_{-0.004}$	$0.194^{+0.004}_{-0.002}$	1.27 ± 0.01	$2.06^{+0.03}_{-0.02}$	$0.2004^{+0.0012}_{-0.0004}$	$3006.8^{+49.9}_{-82.3}$	2.34 ± 0.01	$200.0^{\dagger}$	$0.296^{+0.004}_{-0.003}$
1050020119	$0.48^{+0.01}_{-0.04}$	$0.42^{+0.03}_{-0.01}$	$1.4^{+0.1}_{-0.2}$	$0.872^{+0.004}_{-0.002}$	0.18 ± 0.01	1.5 ± 0.01	$10.9^{+0.1}_{-0.2}$	$0.693^{+0.005}_{-0.022}$	$228.6^{+32.1}_{-17.0}$	$2.78^{+0.02}_{-0.06}$	$2.1^{+1.0}_{-0.1}$	$0.2^{+0.07}_{-0.04}$
1050020121	$0.3821^{+0.0002}_{-0.0003}$	$0.3756^{+0.0001}_{-0.0002}$	$0.8117^{+0.0005}_{-0.0004}$	$0.8628^{+0.0002}_{-0.0003}$	0.2189 ± 0.0001	0.99 ± 0.001	$2.582^{+0.003}_{-0.002}$	$0.3782^{+0.0001}_{-0.0002}$	$1893.73^{+0.83}_{-1.02}$	1.9434 ± 0.0001	$200.0^{\dagger}$	0.0856 ± 0.0001
1050020123	0.351 ± 0.001	$0.382^{+0.001}_{-0.003}$	0.59 ± 0.01	$0.866^{+0.003}_{-0.001}$	$0.164^{+0.002}_{-0.001}$	$1.07^{+0.01}_{-0.02}$	$0.218^{+0.003}_{-0.007}$	0.29 ± 0.01	$313.5^{+12.0}_{-7.2}$	$2.182^{+0.005}_{-0.004}$	$100.8^{+1.3}_{-1.7}$	$0.319^{+0.004}_{-0.002}$
1050020124	$0.388^{+0.002}_{-0.003}$	0.3 ± 0.01	1.06 ± 0.02	$0.859^{+0.003}_{-0.001}$	$0.2^{+0.002}_{-0.003}$	0.94 ± 0.02	$0.64^{+0.03}_{-0.02}$	0.343 ± 0.004	$880.5^{+11.4}_{-16.6}$	2.14 ± 0.01	$200.0^{\dagger}$	$0.126^{+0.002}_{-0.001}$
1050020125	$0.405^{+0.004}_{-0.013}$	0.44 ± 0.01	$0.79^{+0.12}_{-0.02}$	$0.863^{+0.003}_{-0.002}$	$0.185^{+0.014}_{-0.002}$	$1.23^{+0.12}_{-0.01}$	$2.0^{+0.4}_{-0.1}$	$0.33^{+0.01}_{-0.03}$	$1110.2^{+136.4}_{-507.5}$	$2.27^{+0.08}_{-0.02}$	$99.8^{+21.4}_{-36.9}$	$0.23^{+0.07}_{-0.01}$
1050020126	$0.359^{+0.002}_{-0.003}$	0.38 ± 0.01	$0.56^{+0.03}_{-0.02}$	0.87 ± 0.003	$0.206^{+0.002}_{-0.014}$	$1.3^{+0.03}_{-0.02}$	1.8 ± 0.1	$0.221^{+0.001}_{-0.009}$	$2994.6^{+34.6}_{-148.3}$	2.11 ± 0.02	$24.7^{+1.3}_{-2.1}$	0.38 ± 0.01
1050020127	$0.374^{+0.004}_{-0.002}$	0.54 ± 0.02	$0.027^{+0.004}_{-0.013}$	$0.857^{+0.002}_{-0.006}$	0.17 ± 0.01	0.73 ± 0.01	$1.4^{+0.1}_{-0.2}$	$0.338^{+0.001}_{-0.005}$	$1919.0^{+60.1}_{-28.3}$	$1.97^{+0.03}_{-0.02}$	$196.8^{+3.2}_{-11.1}$	0.12 ± 0.01
1050020128	0.332 ± 0.003	0.43 ± 0.01	0.6 ± 0.03	$0.873^{+0.003}_{-0.004}$	$0.163^{+0.006}_{-0.005}$	0.84 ± 0.02	$0.362^{+0.001}_{-0.008}$	$0.367^{+0.012}_{-0.003}$	$140.0^{+2.8}_{-5.6}$	2.16 ± 0.01	$134.0^{+2.6}_{-0.9}$	$0.3^{+0.003}_{-0.004}$
1050020146	$0.47^{+0.01}_{-0.02}$	$0.45^{+0.004}_{-0.012}$	1.3 ± 0.1	$0.864^{+0.001}_{-0.003}$	$0.157^{+0.009}_{-0.003}$	$1.54^{+0.01}_{-0.03}$	$19.4^{+0.3}_{-0.1}$	$0.68^{+0.003}_{-0.02}$	$403.2^{+69.7}_{-7.2}$	$2.79^{+0.01}_{-0.06}$	$2.7^{+0.6}_{-0.7}$	$0.26^{+0.02}_{-0.07}$
1050020182	0.46 ± 0.01	0.444 ± 0.003	$1.41^{+0.09}_{-0.04}$	$0.871^{+0.002}_{-0.003}$	0.17 ± 0.01	$1.5^{+0.02}_{-0.01}$	12.1 ± 0.1	0.7 ± 0.01	$246.6^{+9.9}_{-23.2}$	$2.798^{+0.002}_{-0.022}$	$2.01^{+0.63}_{-0.01}$	$0.16^{+0.03}_{-0.04}$
1050020183	0.327 ± 0.001	0.368 ± 0.001	$0.82^{+0.003}_{-0.004}$	0.867 ± 0.001	$0.202^{+0.002}_{-0.001}$	1.52 ± 0.01	$11.52^{+0.05}_{-0.04}$	0.73 ± 0.001	$190.9^{+0.4}_{-0.5}$	$2.77^{+0.02}_{-0.01}$	$198.1^{+0.9}_{-0.5}$	0.1 ± 0.0005
1050020184	$0.3682^{+0.0001}_{-0.0004}$	$0.3828^{+0.0003}_{-0.0001}$	$0.8639^{+0.0002}_{-0.0006}$	$0.8679^{+0.0003}_{-0.0008}$	$0.21058^{+3e-05}_{-8e-05}$	$1.3666^{+0.0013}_{-0.0005}$	$4.041^{+0.002}_{-0.006}$	$0.503^{+0.0}_{-0.001}$	$469.5^{+0.1}_{-0.4}$	$2.089^{+0.002}_{-0.001}$	$50.42^{+0.01}_{-0.03}$	$0.19974^{+1e-05}_{-4e-05}$
1050020185	0.37 ± 0.001	$0.366^{+0.004}_{-0.005}$	0.7 ± 0.01	0.8647 ± 0.0001	$0.198^{+0.0001}_{-0.0002}$	$0.95^{+0.004}_{-0.003}$	0.78 ± 0.01	$0.365^{+0.001}_{-0.002}$	$969.1^{+9.7}_{-7.1}$	$2.13^{+0.004}_{-0.003}$	$99.9^{+1.7}_{-2.2}$	$0.144^{+0.003}_{-0.002}$
1050020186	0.38 ± 0.01	0.38 ± 0.01	0.37 ± 0.01	$0.861^{+0.004}_{-0.005}$	$0.18^{+0.003}_{-0.006}$	$0.61^{+0.02}_{-0.04}$	$0.54^{+0.05}_{-0.03}$	0.28 ± 0.01	$922.2^{+40.9}_{-54.8}$	$2.14^{+0.01}_{-0.02}$	$200.0^{\dagger}$	0.175 ± 0.002
1050020187	$0.398^{+0.004}_{-0.007}$	$0.414^{+0.003}_{-0.041}$	$0.74^{+0.18}_{-0.03}$	0.867 ± 0.001	0.2 ± 0.004	$1.04^{+0.06}_{-0.03}$	$1.74^{+0.02}_{-0.22}$	$0.37^{+0.01}_{-0.03}$	$1369.3^{+99.5}_{-133.8}$	$2.17^{+0.06}_{-0.02}$	$195.8^{+4.2}_{-26.6}$	$0.17^{+0.04}_{-0.01}$
1050020188	$0.397^{+0.015}_{-0.004}$	$0.39^{+0.03}_{-0.02}$	1.1 ± 0.2	$0.864^{+0.002}_{-0.001}$	$0.185^{+0.002}_{-0.011}$	$1.35^{+0.02}_{-0.07}$	$2.3^{+0.1}_{-0.3}$	0.38 ± 0.02	$152.5^{+346.3}_{-7.8}$	$2.29^{+0.01}_{-0.06}$	$50.6^{+3.5}_{-7.3}$	$0.21^{+0.03}_{-0.02}$
1050020198	$0.3695^{+0.0003}_{-0.0008}$	0.367 ± 0.001	$1.177^{+0.003}_{-0.002}$	$0.868^{+0.002}_{-0.001}$	$0.2166^{+0.0003}_{-0.0008}$	1.19 ± 0.01	2.57 ± 0.01	0.415 ± 0.001	692.2 ± 1.8	$2.256^{+0.002}_{-0.005}$	$200.0^{\dagger}$	$0.1997^{+0.0007}_{-0.0004}$
1050020213	0.397 ± 0.001	$0.36^{+0.002}_{-0.001}$	1.13 ± 0.01	$0.864^{+0.003}_{-0.002}$	$0.164^{+0.002}_{-0.003}$	1.51 ± 0.01	$10.11^{+0.04}_{-0.09}$	0.694 ± 0.003	$142.6^{+0.7}_{-1.4}$	$2.152^{+0.004}_{-0.005}$	$200.0^{\dagger}$	0.111 ± 0.001
1050020214	$0.49^{+0.01}_{-0.02}$	$0.441^{+0.003}_{-0.012}$	1.3 ± 0.1	$0.87^{+0.003}_{-0.008}$	$0.156^{+0.017}_{-0.003}$	$1.58^{+0.02}_{-0.01}$	$18.8^{+0.1}_{-0.3}$	0.68 ± 0.01	$373.6^{+22.2}_{-38.3}$	$2.6^{+0.2}_{-0.1}$	$2.6^{+0.8}_{-0.2}$	0.4 ± 0.1
1050020218	$0.36^{+0.02}_{-0.01}$	0.38 ± 0.02	$0.9^{+0.1}_{-0.2}$	$0.862^{+0.002}_{-0.005}$	0.19 ± 0.01	$1.46^{+0.05}_{-0.01}$	$3.8^{+0.5}_{-0.6}$	$0.52^{+0.05}_{-0.06}$	$124.3^{+30.5}_{-77.4}$	1.9 ± 0.1	$8.3^{+0.8}_{-1.5}$	$0.04^{+0.01}_{-0.04}$
1050020222	$0.344^{+0.004}_{-0.009}$	$0.426^{+0.003}_{-0.002}$	$0.79^{+0.07}_{-0.05}$	0.874 ± 0.002	$0.225^{+0.006}_{-0.002}$	$1.35^{+0.03}_{-0.02}$	2.6 ± 0.1	$0.4^{+0.02}_{-0.03}$	$268.7^{+177.0}_{-248.5}$	$2.33^{+0.04}_{-0.03}$	$161.4^{+24.3}_{-10.0}$	0.22 ± 0.02
1050020224	$0.376^{+0.004}_{-0.003}$	$0.331^{+0.003}_{-0.006}$	0.95 ± 0.02	$0.865^{+0.005}_{-0.002}$	$0.191^{+0.002}_{-0.003}$	$0.85^{+0.02}_{-0.01}$	$1.11^{+0.03}_{-0.01}$	$0.359^{+0.003}_{-0.004}$	$1211.4^{+14.4}_{-19.2}$	$2.05^{+0.03}_{-0.02}$	161.9 ± 2.3	$0.116^{+0.0011}_{-0.0003}$
1050020225	$0.376^{+0.003}_{-0.005}$	$0.366^{+0.008}_{-0.003}$	$0.55^{+0.02}_{-0.01}$	$0.86^{+0.004}_{-0.002}$	0.19 ± 0.003	0.75 ± 0.01	0.72 ± 0.01	$0.338^{+0.006}_{-0.003}$	$876.8^{+40.8}_{-67.3}$	2.1 ± 0.01	$188.1^{+10.1}_{-8.4}$	$0.12^{+0.004}_{-0.003}$
1050020226	$0.48^{+0.02}_{-0.01}$	$0.448^{+0.002}_{-0.003}$	1.4 ± 0.1	$0.867^{+0.004}_{-0.009}$	$0.12^{+0.02}_{-0.01}$	$1.5^{+0.02}_{-0.01}$	$8.9^{+0.1}_{-0.3}$	0.72 ± 0.01	$140.5^{+10.7}_{-17.6}$	2.6 ± 0.1	$2.2^{+0.7}_{-0.1}$	$0.43^{+0.03}_{-0.05}$
1050020229	$0.46^{+0.01}_{-0.04}$	$0.4^{+0.04}_{-0.03}$	$1.0^{+0.3}_{-0.2}$	$0.857^{+0.009}_{-0.005}$	$0.15^{+0.02}_{-0.01}$	$1.36^{+0.05}_{-0.01}$	$8.8^{+1.9}_{-0.9}$	$0.54^{+0.02}_{-0.01}$	$665.9^{+34.0}_{-75.3}$	2.3 ± 0.1	$157.0^{+40.4}_{-94.6}$	0.24 ± 0.04
1050020230	0.41 ± 0.01	$0.426^{+0.02}_{-0.004}$	$0.93^{+0.04}_{-0.02}$	$0.866^{+0.002}_{-0.003}$	0.18 ± 0.01	$1.32^{+0.03}_{-0.04}$	2.3 ± 0.1	$0.21^{+0.02}_{-0.01}$	$1513.3^{+115.9}_{-153.5}$	$2.32^{+0.01}_{-0.02}$	$104.7^{+6.4}_{-14.5}$	0.27 ± 0.02
1050020232	$0.353^{+0.001}_{-0.01}$	$0.4^{+0.01}_{-0.02}$	$0.7^{+0.2}_{-0.1}$	$0.861^{+0.005}_{-0.002}$	$0.195^{+0.002}_{-0.006}$	$0.73^{+0.11}_{-0.01}$	$0.47^{+0.04}_{-0.15}$	$0.31^{+0.03}_{-0.02}$	$813.7^{+76.2}_{-300.6}$	$2.137^{+0.035}_{-0.003}$	$104.9^{+21.0}_{-22.0}$	$0.2^{+0.04}_{-0.01}$
1050020236	$0.48^{+0.01}_{-0.03}$	$0.425^{+0.003}_{-0.044}$	$1.4^{+0.4}_{-0.1}$	$0.87^{+0.004}_{-0.007}$	0.15 ± 0.02	$1.54^{+0.01}_{-0.03}$	$16.0^{+0.3}_{-0.7}$	0.66 ± 0.01	$421.6^{+46.7}_{-54.1}$	$2.6^{+0.1}_{-0.4}$	3.2 ± 0.9	$0.34^{+0.02}_{-0.14}$
1050020241	0.359 ± 0.002	$0.35^{+0.015}_{-0.004}$	$0.48^{+0.02}_{-0.01}$	$0.875^{+0.003}_{-0.005}$	$0.1963^{+0.0091}_{-0.0003}$	$1.233^{+0.003}_{-0.031}$	$0.69^{+0.03}_{-0.04}$	$0.263^{+0.004}_{-0.003}$	$3547.7^{+70.4}_{-73.6}$	$1.981^{+0.015}_{-0.004}$	$22.8^{+0.3}_{-1.4}$	$0.328^{+0.011}_{-0.004}$
1050020242	0.374 ± 0.001	$0.366^{+0.003}_{-0.002}$	0.56 ± 0.01	0.865 ± 0.002	$0.179^{+0.002}_{-0.001}$	$0.643^{+0.002}_{-0.003}$	$0.59^{+0.004}_{-0.005}$	0.283 ± 0.001	$1532.6^{+22.5}_{-9.1}$	2.067 ± 0.002	$100.0^{+0.4}_{-0.7}$	$0.2419^{+0.0004}_{-0.0008}$
1050020243	$0.37^{+0.001}_{-0.004}$	0.35 ± 0.01	$0.5^{+0.02}_{-0.03}$	$0.862^{+0.004}_{-0.002}$	0.18 ± 0.01	$0.61^{+0.02}_{-0.03}$	$0.58^{+0.06}_{-0.04}$	0.24 ± 0.01	$2555.3^{+24.8}_{-64.1}$	$2.07^{+0.01}_{-0.02}$	$64.2^{+0.2}_{-0.1}$	$0.243^{+0.005}_{-0.001}$
1050020244	0.42 ± 0.01	$0.38^{+0.05}_{-0.01}$	0.4 ± 0.1	$0.864^{+0.004}_{-0.003}$	0.21 ± 0.01	$0.85^{+0.02}_{-0.01}$	$2.7^{+0.1}_{-0.5}$	$0.367^{+0.004}_{-0.011}$	$2315.2^{+120.9}_{-157.6}$	$1.84^{+0.12}_{-0.01}$	$180.8^{+19.2}_{-9.6}$	$0.08^{+0.04}_{-0.01}$
1050020252	$0.43^{+0.02}_{-0.01}$	$0.44^{+0.01}_{-0.02}$	0.5 ± 0.1	$0.864^{+0.001}_{-0.006}$	$0.157^{+0.011}_{-0.004}$	$1.33^{+0.04}_{-0.03}$	$12.1^{+0.9}_{-1.0}$	0.54 ± 0.01	$992.3^{+90.3}_{-96.5}$	$1.79^{+0.07}_{-0.01}$	$50.2^{+8.4}_{-5.8}$	$0.24^{+0.03}_{-0.02}$
1050020255	$0.472^{+0.005}_{-0.014}$	$0.4424^{+0.0005}_{-0.0026}$	1.5 ± 0.1	$0.875^{+0.001}_{-0.006}$	$0.146^{+0.014}_{-0.002}$	1.58 ± 0.01	$17.7^{+0.1}_{-0.3}$	0.72 ± 0.01	$334.8^{+8.1}_{-34.9}$	$2.77^{+0.03}_{-0.14}$	$2.2^{+0.6}_{-0.2}$	$0.22^{+0.08}_{-0.05}$
1050020256	0.47 ± 0.01	$0.446^{+0.001}_{-0.004}$	1.4 ± 0.1	0.873 ± 0.003	0.16 ± 0.01	$1.55^{+0.01}_{-0.02}$	$11.2^{+0.1}_{-0.2}$	$0.74^{+0.01}_{-0.02}$	$170.0^{+19.1}_{-14.9}$	$2.795^{+0.005}_{-0.055}$	$2.3^{+0.6}_{-0.3}$	$0.36^{+0.06}_{-0.04}$
1050020257	$0.466^{+0.003}_{-0.014}$	$0.44^{+0.001}_{-0.002}$	$1.44^{+0.05}_{-0.06}$	$0.874^{+0.001}_{-0.003}$	$0.158^{+0.012}_{-0.004}$	1.56 ± 0.01	14.8 ± 0.1	0.72 ± 0.01	$275.6^{+12.5}_{-19.3}$	$2.78^{+0.02}_{-0.1}$	$2.1^{+0.3}_{-0.1}$	$0.15^{+0.07}_{-0.02}$
1050020269	$0.49^{+0.01}_{-0.02}$	$0.4^{+0.03}_{-0.01}$	$1.7^{+0.1}_{-0.3}$	$0.871^{+0.005}_{-0.003}$	$0.16^{+0.02}_{-0.01}$	$1.55^{+0.02}_{-0.01}$	$10.7^{+0.1}_{-0.4}$	$0.7^{+0.02}_{-0.01}$	$197.4^{+2.3}_{-41.5}$	$2.77^{+0.03}_{-0.2}$	$2.6^{+0.5}_{-0.6}$	$0.33^{+0.11}_{-0.01}$
4701010101	$0.39^{+0.03}_{-0.01}$	0.45 ± 0.01	$0.6^{+0.1}_{-0.2}$	$0.871^{+0.002}_{-0.006}$	0.21 ± 0.01	$0.98^{+0.01}_{-0.06}$	$2.3^{+0.3}_{-0.2}$	$0.358^{+0.029}_{-0.004}$	$2109.4^{+66.5}_{-194.3}$	1.9 ± 0.1	$183.7^{+15.8}_{-17.2}$	$0.05^{+0.01}_{-0.02}$

Table B2
(Continued)

OBSID	TBABS	EDGE 1		EDGE 2		BBODY		DISKBB		CUTOFFPL		
	$N_{\rm H}$ (10^{22} cm^{-2})	E (keV)	$\tau_{\rm max}$	E (keV)	$\tau_{\rm max}$	kT (keV)	$k_{\rm BB}$ (10^{-3})	kT (keV)	$k_{\rm DBB}$	Γ	$E_{\rm cutoff}$ (keV)	$k_{\rm PL}$
4701010201	$0.393^{+0.008}_{-0.005}$	$0.437^{+0.003}_{-0.002}$	$1.24^{+0.04}_{-0.03}$	0.872 ± 0.001	0.19 ± 0.01	$1.44^{+0.04}_{-0.02}$	1.9 ± 0.1	0.3 ± 0.04	$404.1^{+223.5}_{-69.6}$	$2.49^{+0.03}_{-0.04}$	$123.8^{+16.3}_{-44.1}$	$0.28^{+0.02}_{-0.01}$
4701010301	0.326 ± 0.005	0.4 ± 0.01	0.47 ± 0.02	0.86 ± 0.01	$0.138^{+0.006}_{-0.003}$	$0.47^{+0.02}_{-0.01}$	0.47 ± 0.01	0.55 ± 0.02	$22.4^{+1.7}_{-1.4}$	2.03 ± 0.01	$67.4^{+2.3}_{-1.1}$	$0.189^{+0.003}_{-0.002}$
4701010302	$0.293^{+0.003}_{-0.001}$	$0.46^{+0.001}_{-0.002}$	$0.29^{+0.008}_{-0.004}$	$0.875^{+0.003}_{-0.001}$	$0.145^{+0.001}_{-0.002}$	$0.586^{+0.005}_{-0.001}$	$1.28^{+0.01}_{-0.02}$	$0.3709^{+0.0026}_{-0.0004}$	$543.4^{+3.9}_{-8.0}$	1.77 ± 0.01	$101.4^{+3.0}_{-1.7}$	$0.1164^{+0.0015}_{-0.0004}$
4701010401	$0.365^{+0.003}_{-0.002}$	$0.375^{+0.004}_{-0.011}$	$0.48^{+0.02}_{-0.01}$	$0.866^{+0.003}_{-0.002}$	$0.162^{+0.007}_{-0.002}$	$1.11^{+0.03}_{-0.01}$	0.2 ± 0.01	$0.248^{+0.006}_{-0.005}$	$784.5^{+37.0}_{-17.5}$	2.19 ± 0.01	$100.3^{+1.1}_{-1.0}$	$0.321^{+0.002}_{-0.001}$
5050020204	$0.321^{+0.003}_{-0.002}$	0.358 ± 0.004	0.72 ± 0.02	$0.876^{+0.003}_{-0.005}$	$0.199^{+0.008}_{-0.003}$	1.14 ± 0.03	1.39 ± 0.04	$0.243^{+0.006}_{-0.004}$	$3003.5^{+82.9}_{-72.4}$	2.08 ± 0.01	$59.3^{+1.0}_{-0.7}$	$0.215^{+0.003}_{-0.002}$
5050020206	$0.482^{+0.004}_{-0.029}$	$0.413^{+0.033}_{-0.002}$	$1.4^{+0.1}_{-0.2}$	0.867 ± 0.004	$0.14^{+0.02}_{-0.01}$	$1.56^{+0.02}_{-0.01}$	$19.4^{+0.2}_{-0.4}$	0.69 ± 0.01	$398.4^{+21.1}_{-37.9}$	2.7 ± 0.1	$2.3^{+1.5}_{-0.3}$	$0.01^{+0.07}_{-0.01}$
5050020208	0.317 ± 0.002	$0.42^{+0.003}_{-0.007}$	$0.563^{+0.015}_{-0.002}$	$0.875^{+0.001}_{-0.002}$	$0.215^{+0.008}_{-0.002}$	1.16 ± 0.01	2.8 ± 0.1	$0.35^{+0.02}_{-0.03}$	$217.3^{+140.0}_{-60.7}$	2.14 ± 0.01	$166.5^{+33.5}_{-11.7}$	$0.273^{+0.001}_{-0.015}$
5050020221	0.47 ± 0.01	$0.39^{+0.04}_{-0.01}$	$1.791^{+0.004}_{-0.516}$	$0.877^{+0.005}_{-0.007}$	0.14 ± 0.01	$1.5^{+0.01}_{-0.02}$	$15.4^{+0.1}_{-0.7}$	$0.64^{+0.01}_{-0.03}$	$410.1^{+69.7}_{-41.6}$	$2.3^{+0.1}_{-0.2}$	$2.2^{+1.3}_{-0.2}$	0.2 ± 0.1
5050020222	$0.3079^{+0.0022}_{-0.0003}$	0.4 ± 0.01	$0.74^{+0.04}_{-0.07}$	$0.874^{+0.001}_{-0.003}$	$0.2275^{+0.0004}_{-0.001}$	$1.08^{+0.01}_{-0.02}$	0.8 ± 0.1	$0.254^{+0.003}_{-0.002}$	$2977.4^{+101.5}_{-100.5}$	$1.97^{+0.02}_{-0.01}$	$29.1^{+5.7}_{-2.8}$	$0.235^{+0.002}_{-0.006}$

Table B3
4U 0614+091 Results of Reflection Modeling: Reflection Parameters

OBSID	RELCONV		XILLVERCO					χ^2 (dof)
	q	$R_{\rm in}$ ($R_{\rm ISCO}$)	$A_{\rm CO}$	frac	$kT_{\rm xill}$ (10^{-2} keV)	$k_{\rm xillverCO}$ (10^{-9})	$\log \xi$	
1050020115	$3.8^{+0.2}_{-0.3}$	$1.03^{+0.08}_{-0.03}$	3.3 ± 0.6	$0.011^{+0.002}_{-0.001}$	$9.992^{+0.004}_{-0.008}$	$50.5^{+0.7}_{-5.3}$	2.14 ± 0.02	292(127)
1050020116	$2.842^{+0.084}_{-0.001}$	$1.002^{+0.197}_{-0.002}$	$24.6^{+1.3}_{-1.8}$	$0.05^{+0.014}_{-0.005}$	$10.18^{+0.11}_{-0.04}$	$4.1^{+0.5}_{-0.4}$	2.84 ± 0.04	307(125)
1050020117	$2.64^{+0.08}_{-0.04}$	$1.00089^{+3e-05}_{-2e-05}$	$19.8^{+0.4}_{-0.2}$	0.05 ± 0.001	$10.048^{+0.005}_{-0.004}$	$6.41^{+0.04}_{-0.08}$	2.82 ± 0.01	218(121)
1050020118	2.57 ± 0.01	$1.004^{+0.024}_{-0.004}$	$290.1^{+2.2}_{-0.8}$	0.022 ± 0.001	$11.14^{+0.04}_{-0.03}$	$1.22^{+0.02}_{-0.03}$	2.64 ± 0.01	208(118)
1050020119	$3.0^{+0.3}_{-0.2}$	1.1 ± 0.1	$14.0^{+6.1}_{-2.9}$	$0.022^{+0.001}_{-0.004}$	10.014 ± 0.002	43.3 ± 3.1	2.5 ± 0.1	265(126)
1050020121	2.589 ± 0.001	$1.0001^{+0.0002}_{-0.0001}$	$13.73^{+0.004}_{-0.005}$	$0.04963 \pm 1e-05$	10.024 ± 0.001	8.908 ± 0.002	2.8113 ± 0.0001	183(121)
1050020123	2.62 ± 0.01	$1.001^{+0.038}_{-0.001}$	$59.3^{+1.5}_{-1.2}$	$0.38^{+0.006}_{-0.001}$	$6.45^{+0.05}_{-0.1}$	$1.69^{+0.04}_{-0.02}$	2.93 ± 0.01	307(132)
1050020124	2.52 ± 0.03	$1.01^{+0.02}_{-0.01}$	$17.1^{+0.3}_{-0.4}$	0.118 ± 0.001	9.9 ± 0.1	4.6 ± 0.1	3.17 ± 0.01	271(132)
1050020125	$2.68^{+0.09}_{-0.03}$	$1.04^{+0.09}_{-0.04}$	$15.0^{+2.3}_{-1.0}$	$0.033^{+0.001}_{-0.003}$	$10.035^{+0.006}_{-0.002}$	$14.6^{+1.2}_{-0.8}$	2.63 ± 0.04	446(132)
1050020126	$2.76^{+0.03}_{-0.11}$	$1.21^{+0.02}_{-0.09}$	$248.8^{+7.3}_{-4.9}$	$0.0159^{+0.00019}_{-4e-05}$	$10.41^{+0.03}_{-0.02}$	4.2 ± 0.1	2.383 ± 0.002	218(123)
1050020127	$2.6^{+0.1}_{-0.2}$	$1.4^{+0.1}_{-0.4}$	$58.3^{+5.2}_{-2.5}$	$0.58^{+0.06}_{-0.04}$	8.9 ± 0.2	1.0 ± 0.1	3.66 ± 0.03	263(130)
1050020128	$2.63^{+0.05}_{-0.02}$	$1.001^{+0.003}_{-0.001}$	$44.6^{+0.5}_{-0.9}$	0.088 ± 0.001	$9.9^{+0.1}_{-0.4}$	$1.4^{+0.2}_{-0.1}$	3.04 ± 0.03	259(125)
1050020146	$3.06^{+0.04}_{-0.23}$	$1.05^{+0.21}_{-0.05}$	$5.83^{+7.05}_{-0.81}$	$0.026^{+0.003}_{-0.001}$	10.003 ± 0.001	$39.1^{+0.5}_{-4.8}$	2.53 ± 0.02	276(130)
1050020182	3.3 ± 0.2	$1.02^{+0.09}_{-0.02}$	$8.4^{+2.9}_{-2.8}$	$0.022^{+0.001}_{-0.002}$	10.016 ± 0.001	$44.4^{+2.5}_{-1.5}$	2.46 ± 0.04	496(135)
1050020183	2.58 ± 0.01	1.001 ± 0.001	$275.2^{+0.6}_{-0.5}$	$0.01405^{+4e-05}_{-3e-05}$	$11.03^{+0.06}_{-0.03}$	2.2 ± 0.1	2.43 ± 0.003	650(143)
1050020184	$2.6584^{+0.0004}_{-0.0011}$	$1.00003^{+0.0001}_{-3e-05}$	$20.435^{+0.009}_{-0.003}$	$0.06391^{+1e-05}_{-3e-05}$	$10.079^{+0.002}_{-0.001}$	$5.67^{+0.002}_{-0.005}$	2.9306 ± 0.0002	285(126)
1050020185	$2.61^{+0.01}_{-0.02}$	$1.05^{+0.03}_{-0.04}$	$23.0^{+0.3}_{-0.2}$	$0.1274^{+0.0002}_{-0.0003}$	9.998 ± 0.001	$3.01^{+0.02}_{-0.03}$	3.216 ± 0.001	177(127)
1050020186	2.48 ± 0.04	$1.11^{+0.01}_{-0.02}$	$19.5^{+1.6}_{-0.9}$	$0.09^{+0.01}_{-0.0}$	$9.8^{+0.2}_{-0.1}$	$2.6^{+0.2}_{-0.4}$	3.02 ± 0.03	177(124)
1050020187	2.65 ± 0.03	$1.01^{+0.18}_{-0.01}$	$15.1^{+2.7}_{-0.5}$	$0.037^{+0.003}_{-0.002}$	$10.02^{+0.02}_{-0.01}$	$10.7^{+0.4}_{-1.9}$	2.69 ± 0.03	303(129)
1050020188	$2.68^{+0.04}_{-0.01}$	$1.01^{+0.13}_{-0.01}$	$15.0^{+0.5}_{-1.6}$	$0.035^{+0.001}_{-0.005}$	$10.057^{+0.003}_{-0.02}$	$12.8^{+2.7}_{-0.7}$	2.7 ± 0.1	236(130)
1050020198	2.65 ± 0.01	$1.001^{+0.003}_{-0.001}$	$19.8^{+0.04}_{-0.08}$	0.0495 ± 0.0002	$10.049^{+0.001}_{-0.002}$	$6.39^{+0.01}_{-0.02}$	2.815 ± 0.001	218(121)
1050020213	2.74 ± 0.02	1.115 ± 0.003	13.9 ± 0.1	$0.0435^{+0.0002}_{-0.0003}$	10.089 ± 0.001	12.5 ± 0.1	2.765 ± 0.003	293(133)
1050020214	3.1 ± 0.2	$1.04^{+0.17}_{-0.04}$	$5.1^{+2.8}_{-0.5}$	$0.018^{+0.003}_{-0.002}$	$9.6^{+0.2}_{-0.3}$	$55.6^{+2.7}_{-8.2}$	2.29 ± 0.05	303(131)
1050020218	2.6 ± 0.1	$1.01^{+0.16}_{-0.01}$	$14.8^{+0.6}_{-1.9}$	$0.051^{+0.005}_{-0.002}$	$10.09^{+0.01}_{-0.02}$	$7.7^{+1.1}_{-0.3}$	2.84 ± 0.02	202(118)
1050020222	$2.6^{+0.02}_{-0.0}$	$1.02^{+0.11}_{-0.02}$	$31.2^{+2.9}_{-1.1}$	0.06 ± 0.01	$10.14^{+0.03}_{-0.01}$	$4.2^{+0.3}_{-0.4}$	2.9 ± 0.1	257(122)
1050020224	$2.59^{+0.04}_{-0.05}$	$1.01^{+0.05}_{-0.01}$	16.5 ± 0.3	$0.069^{+0.002}_{-0.001}$	$9.99^{+0.01}_{-0.11}$	$5.0^{+0.2}_{-0.1}$	2.95 ± 0.01	169(122)
1050020225	2.57 ± 0.03	1.1 ± 0.02	$15.2^{+0.4}_{-0.3}$	0.098 ± 0.001	9.1 ± 0.05	5.0 ± 0.1	2.94 ± 0.01	191(128)
1050020226	3.6 ± 0.2	$1.03^{+0.13}_{-0.03}$	$3.0^{+0.3}_{-0.5}$	$0.0103^{+0.0003}_{-0.0002}$	10.011 ± 0.001	$48.7^{+2.2}_{-3.6}$	2.13 ± 0.01	369(130)
1050020229	2.8 ± 0.2	1.2 ± 0.2	$9.0^{+2.6}_{-2.2}$	$0.027^{+0.002}_{-0.003}$	$9.8^{+0.2}_{-0.3}$	$28.4^{+4.3}_{-4.0}$	2.5 ± 0.1	271(128)
1050020230	$2.76^{+0.1}_{-0.05}$	1.1 ± 0.1	$15.9^{+1.3}_{-1.2}$	$0.029^{+0.001}_{-0.003}$	$10.046^{+0.003}_{-0.005}$	$14.8^{+2.0}_{-1.2}$	2.59 ± 0.04	358(131)
1050020232	$2.58^{+0.03}_{-0.01}$	$1.03^{+0.08}_{-0.03}$	$20.1^{+3.2}_{-0.4}$	$0.08^{+0.02}_{-0.01}$	10.0 ± 0.02	$3.0^{+0.2}_{-0.5}$	3.0 ± 0.1	187(127)
1050020236	3.1 ± 0.2	$1.05^{+0.13}_{-0.05}$	$5.5^{+5.05}_{-0.94}$	$0.02^{+0.005}_{-0.001}$	$9.87^{+0.06}_{-0.04}$	$47.3^{+0.7}_{-9.5}$	2.4 ± 0.03	242(127)
1050020241	$2.66^{+0.03}_{-0.13}$	$1.15^{+0.01}_{-0.15}$	$298.7^{+6.4}_{-3.7}$	$0.0238^{+0.0008}_{-0.0003}$	$10.82^{+0.02}_{-0.12}$	$1.42^{+0.12}_{-0.02}$	2.62 ± 0.01	184(120)
1050020242	$2.52^{+0.03}_{-0.02}$	$1.0028^{+0.0004}_{-0.0003}$	21.2 ± 0.1	0.07 ± 0.001	$9.99^{+0.01}_{-0.04}$	$3.46^{+0.02}_{-0.03}$	2.96 ± 0.01	192(131)
1050020243	$2.54^{+0.04}_{-0.01}$	$1.08^{+0.03}_{-0.01}$	$25.0^{+1.7}_{-1.1}$	$0.099^{+0.003}_{-0.004}$	$9.7^{+0.1}_{-0.2}$	2.3 ± 0.1	3.06 ± 0.02	152(130)
1050020244	$2.61^{+0.05}_{-0.06}$	1.1 ± 0.1	$12.7^{+1.3}_{-0.6}$	$0.043^{+0.002}_{-0.005}$	$9.929^{+0.002}_{-0.008}$	11.9 ± 1.2	2.7 ± 0.1	212(131)
1050020252	2.7 ± 0.1	$1.1^{+0.3}_{-0.1}$	$10.85^{+0.923}_{-1.001}$	$0.036^{+0.004}_{-0.002}$	$10.004^{+0.001}_{-0.01}$	$20.3^{+1.7}_{-2.3}$	2.67 ± 0.03	499(138)
1050020255	$3.5^{+0.2}_{-0.3}$	1.1 ± 0.1	$5.8^{+2.4}_{-1.0}$	$0.02^{+0.001}_{-0.002}$	$10.0137^{+0.0008}_{-0.0004}$	$59.9^{+0.3}_{-5.6}$	2.42 ± 0.04	413(134)
1050020256	$3.7^{+0.7}_{-0.3}$	$1.01^{+0.2}_{-0.01}$	$5.1^{+1.9}_{-0.4}$	0.018 ± 0.002	10.017 ± 0.001	$53.4^{+3.5}_{-4.4}$	2.4 ± 0.1	338(131)
1050020257	$3.5^{+0.1}_{-0.3}$	$1.02^{+0.06}_{-0.02}$	$6.3^{+3.3}_{-1.4}$	0.021 ± 0.001	10.018 ± 0.001	$54.5^{+0.4}_{-3.8}$	2.44 ± 0.03	663(143)
1050020269	3.4 ± 0.3	$1.1^{+0.2}_{-0.1}$	$5.0^{+3.5}_{-0.2}$	$0.021^{+0.001}_{-0.004}$	10.009 ± 0.001	$44.8^{+3.0}_{-4.2}$	2.4 ± 0.1	189(125)
4701010101	2.7 ± 0.1	$1.01^{+0.12}_{-0.01}$	$11.4^{+0.3}_{-1.9}$	$0.032^{+0.001}_{-0.003}$	$10.029^{+0.001}_{-0.042}$	$13.5^{+2.7}_{-0.3}$	2.62 ± 0.04	319(127)
4701010201	2.9 ± 0.1	$1.01^{+0.06}_{-0.01}$	$14.4^{+1.1}_{-2.1}$	0.019 ± 0.001	$10.008^{+0.002}_{-0.005}$	$17.2^{+2.2}_{-1.0}$	2.39 ± 0.03	507(128)
4701010301	2.6 ± 0.1	$1.5^{+0.2}_{-0.1}$	$33.4^{+2.2}_{-2.8}$	$0.038^{+0.0004}_{-0.0011}$	9.9 ± 0.1	1.3 ± 0.1	2.67 ± 0.01	125(117)
4701010302	$2.48^{+0.01}_{-0.03}$	$1.004^{+0.055}_{-0.004}$	$30.5^{+0.5}_{-0.9}$	$0.04^{+0.002}_{-0.003}$	$10.005^{+0.002}_{-0.031}$	1.2 ± 0.1	2.72 ± 0.03	182(124)
4701010401	$2.59^{+0.03}_{-0.02}$	$1.063^{+0.01}_{-0.003}$	$60.7^{+1.1}_{-0.6}$	0.4 ± 0.01	6.6 ± 0.1	$1.57^{+0.05}_{-0.04}$	2.99 ± 0.02	287(132)
5050020204	$2.6^{+0.05}_{-0.04}$	$1.02^{+0.05}_{-0.02}$	$255.4^{+5.5}_{-5.2}$	0.021 ± 0.0002	11.3 ± 0.1	$0.94^{+0.07}_{-0.04}$	2.64 ± 0.01	243(119)
5050020206	$2.9^{+0.4}_{-0.1}$	$1.04^{+0.27}_{-0.04}$	$5.0^{+0.5}_{-0.2}$	$0.028^{+0.002}_{-0.004}$	$10.0113^{+0.0026}_{-0.0001}$	$42.9^{+2.7}_{-7.0}$	2.6 ± 0.1	383(129)
5050020208	$2.684^{+0.037}_{-0.003}$	$1.002^{+0.124}_{-0.002}$	$198.9^{+6.5}_{-22.3}$	$0.0147^{+0.0015}_{-0.0003}$	10.4 ± 0.1	4.6 ± 0.6	2.35 ± 0.01	475(128)
5050020221	$3.4^{+0.2}_{-0.3}$	1.1 ± 0.1	$4.79^{+2.02}_{-0.46}$	$0.017^{+0.004}_{-0.001}$	10.008 ± 0.003	$45.1^{+1.2}_{-5.5}$	2.33 ± 0.04	425(129)
5050020222	2.69 ± 0.02	$1.005^{+0.072}_{-0.004}$	$257.3^{+7.8}_{-18.8}$	$0.0143^{+0.0014}_{-0.0002}$	10.4 ± 0.1	$2.4^{+0.6}_{-0.3}$	2.34 ± 0.01	331(124)

Table B4
4U 0614+091 Results of Reflection Modeling: Calculated Fluxes and Equivalent Widths

	FLUXES (10^{-10} ergs cm^{-2} s^{-1})						
OBSID	Blackbody	Disk Blackbody	Power Law	XILLVERCO	Total	Line Energy (keV)	EW (eV)
1050020115	12.32 ± 0.03	12.32 ± 0.01	8.05 ± 0.02	11.42 ± 0.03	36.76 ± 0.02	$0.684^{+0.002}_{-0.003}$	39.1 ± 2.9
1050020116	5.62 ± 0.03	5.57 ± 0.01	19.76 ± 0.04	13.95 ± 0.02	42.38 ± 0.03	$0.688^{+0.004}_{-0.003}$	54.1 ± 0.8
1050020117	2.15 ± 0.02	3.01 ± 0.01	9.98 ± 0.02	10.16 ± 0.02	23.15 ± 0.02	$0.6931^{+0.0104}_{-0.0003}$	$15.8^{+13.1}_{-7.6}$
1050020118	1.73 ± 0.02	0.36 ± 0.01	13.58 ± 0.02	6.18 ± 0.02	20.68 ± 0.02	$0.692^{+0.002}_{-0.004}$	$58.5^{+0.9}_{-0.8}$
1050020119	9.15 ± 0.02	9.27 ± 0.01	3.8 ± 0.02	13.83 ± 0.02	29.57 ± 0.02	$0.695^{+0.003}_{-0.002}$	52.7 ± 0.8
1050020121	2.15 ± 0.02	5.34 ± 0.02	6.56 ± 0.04	13.59 ± 0.03	25.81 ± 0.03	$0.694^{+0.003}_{-0.004}$	53.8 ± 1.1
1050020123	0.18 ± 0.01	0.24 ± 0.01	16.75 ± 0.01	2.66 ± 0.01	18.94 ± 0.01	$0.684^{+0.004}_{-0.003}$	$33.5^{+8.2}_{-8.1}$
1050020124	0.54 ± 0.01	1.57 ± 0.01	7.32 ± 0.01	13.06 ± 0.01	21.37 ± 0.01	$0.686^{+0.003}_{-0.002}$	$50.4^{+0.5}_{-0.4}$
1050020125	1.96 ± 0.01	0.73 ± 0.01	13.59 ± 0.01	13.11 ± 0.01	26.1 ± 0.01	$0.743^{+0.003}_{-0.002}$	120.3 ± 0.5
1050020126	1.54 ± 0.02	0.58 ± 0.01	17.61 ± 0.02	7.23 ± 0.02	25.44 ± 0.02	0.667 ± 0.002	48.4 ± 1.2
1050020127	1.17 ± 0.01	3.17 ± 0.01	9.46 ± 0.02	8.81 ± 0.02	22.2 ± 0.01	$0.689^{+0.002}_{-0.003}$	53.0 ± 0.7
1050020128	0.3 ± 0.01	0.37 ± 0.01	16.5 ± 0.02	2.49 ± 0.01	18.6 ± 0.02	$0.687^{+0.006}_{-0.002}$	$49.7^{+50.1}_{-16.1}$
1050020146	16.36 ± 0.04	15.51 ± 0.02	4.53 ± 0.03	13.71 ± 0.03	42.04 ± 0.03	$0.692^{+0.002}_{-0.003}$	51.5 ± 1.8
1050020182	10.09 ± 0.02	10.35 ± 0.01	3.26 ± 0.01	16.08 ± 0.02	32.01 ± 0.01	$0.6856^{+0.0004}_{-0.0005}$	55.4 ± 0.8
1050020183	9.64 ± 0.02	9.73 ± 0.01	3.39 ± 0.01	7.47 ± 0.01	28.48 ± 0.01	0.693 ± 0.001	49.9 ± 0.4
1050020184	3.38 ± 0.03	4.79 ± 0.02	10.91 ± 0.03	14.28 ± 0.03	31.15 ± 0.02	0.695 ± 0.003	$47.4^{+19.9}_{-3.6}$
1050020185	0.65 ± 0.01	2.31 ± 0.01	8.04 ± 0.02	9.43 ± 0.02	19.28 ± 0.01	0.694 ± 0.003	61.9 ± 1.7
1050020186	0.46 ± 0.01	0.62 ± 0.01	10.19 ± 0.02	5.22 ± 0.01	15.9 ± 0.01	$0.691^{+0.001}_{-0.004}$	48.2 ± 1.0
1050020187	1.36 ± 0.01	3.02 ± 0.01	10.7 ± 0.02	10.94 ± 0.02	23.96 ± 0.02	$0.694^{+0.003}_{-0.001}$	51.5 ± 1.2
1050020188	1.88 ± 0.02	0.87 ± 0.01	9.53 ± 0.02	15.9 ± 0.02	25.42 ± 0.02	$0.676^{+0.001}_{-0.005}$	51.9 ± 1.2
1050020198	2.15 ± 0.02	3.01 ± 0.01	9.98 ± 0.02	10.16 ± 0.02	23.15 ± 0.02	$0.689^{+0.003}_{-0.004}$	45.4 ± 1.4
1050020213	5.65 ± 0.03	1.67 ± 0.02	5.46 ± 0.03	34.05 ± 0.02	44.1 ± 0.02	0.763 ± 0.001	105.4 ± 2.3
1050020214	15.64 ± 0.04	14.02 ± 0.02	8.35 ± 0.02	13.13 ± 0.03	43.09 ± 0.03	$0.696^{+0.002}_{-0.003}$	46.9 ± 0.7
1050020218	3.23 ± 0.02	1.02 ± 0.01	0.63 ± 0.02	18.61 ± 0.01	21.67 ± 0.01	$0.695^{+0.002}_{-0.003}$	51.6 ± 0.8
1050020222	2.18 ± 0.02	0.53 ± 0.01	10.17 ± 0.02	11.25 ± 0.02	22.01 ± 0.02	$0.691^{+0.004}_{-0.001}$	51.6 ± 0.8
1050020224	0.93 ± 0.01	2.67 ± 0.01	7.45 ± 0.02	8.99 ± 0.02	18.95 ± 0.02	0.692 ± 0.002	66.2 ± 3.1
1050020225	0.59 ± 0.01	1.47 ± 0.01	7.38 ± 0.01	8.74 ± 0.01	17.35 ± 0.01	$0.704^{+0.012}_{-0.003}$	37.0 ± 2.5
1050020226	7.35 ± 0.02	6.43 ± 0.01	7.69 ± 0.02	12.47 ± 0.02	26.89 ± 0.02	$0.762^{+0.003}_{-0.004}$	119.1 ± 1.9
1050020229	8.35 ± 0.04	10.09 ± 0.02	10.76 ± 0.03	15.68 ± 0.03	40.51 ± 0.03	$0.69322^{+0.00015}_{-0.00001}$	$47.7^{+1.2}_{-1.1}$
1050020230	1.97 ± 0.02	0.18 ± 0.01	12.61 ± 0.02	14.2 ± 0.02	25.69 ± 0.02	$0.695^{+0.004}_{-0.002}$	54.4 ± 0.6
1050020232	0.34 ± 0.01	0.76 ± 0.01	11.64 ± 0.01	5.18 ± 0.01	16.7 ± 0.01	$0.689^{+0.005}_{-0.002}$	59.6 ± 1.9
1050020236	13.19 ± 0.04	12.88 ± 0.02	6.01 ± 0.03	14.44 ± 0.04	39.5 ± 0.03	$0.691^{+0.003}_{-0.004}$	48.8 ± 0.9
1050020241	0.58 ± 0.03	1.81 ± 0.02	17.35 ± 0.03	5.53 ± 0.02	24.13 ± 0.03	$0.693^{+0.005}_{-0.003}$	$52.4^{+1.1}_{-1.2}$
1050020242	0.48 ± 0.01	1.09 ± 0.01	14.66 ± 0.02	6.1 ± 0.01	21.4 ± 0.01	0.688 ± 0.002	51.1 ± 2.4
1050020243	0.49 ± 0.01	0.78 ± 0.01	14.26 ± 0.02	5.01 ± 0.01	19.8 ± 0.01	$0.686^{+0.003}_{-0.002}$	46.6 ± 1.4
1050020244	2.01 ± 0.01	5.24 ± 0.01	8.7 ± 0.02	12.53 ± 0.02	27.0 ± 0.02	0.76 ± 0.001	120.4 ± 2.8
1050020252	10.38 ± 0.03	14.27 ± 0.01	20.56 ± 0.04	21.66 ± 0.03	63.29 ± 0.03	$0.717^{+0.002}_{-0.006}$	25.0 ± 1.4
1050020255	14.52 ± 0.03	14.13 ± 0.01	6.45 ± 0.02	20.03 ± 0.02	45.69 ± 0.02	$0.698^{+0.002}_{-0.001}$	76.4 ± 7.5
1050020256	9.42 ± 0.03	9.26 ± 0.02	6.54 ± 0.02	18.01 ± 0.03	34.11 ± 0.02	0.693 ± 0.002	56.4 ± 1.6
1050020257	12.23 ± 0.02	12.08 ± 0.01	5.31 ± 0.01	19.38 ± 0.02	40.05 ± 0.01	$0.695^{+0.001}_{-0.002}$	49.5 ± 1.0
1050020269	8.84 ± 0.03	7.8 ± 0.02	7.11 ± 0.02	15.32 ± 0.03	31.8 ± 0.03	$0.696^{+0.004}_{-0.002}$	$52.2^{+2.0}_{-1.9}$
4701010101	1.97 ± 0.01	4.88 ± 0.01	4.05 ± 0.02	14.56 ± 0.02	23.4 ± 0.02	0.694 ± 0.002	53.8 ± 0.6
4701010201	1.57 ± 0.01	0.53 ± 0.01	11.08 ± 0.01	7.76 ± 0.01	17.53 ± 0.01	$0.69^{+0.004}_{-0.002}$	53.9 ± 1.4
4701010301	0.37 ± 0.01	0.41 ± 0.01	11.49 ± 0.02	0.85 ± 0.01	12.71 ± 0.02	$0.677^{+0.005}_{-0.007}$	36.8 ± 3.7
4701010302	1.06 ± 0.01	1.42 ± 0.01	11.52 ± 0.02	1.13 ± 0.01	14.72 ± 0.01	$0.676^{+0.005}_{-0.004}$	37.6 ± 0.8
4701010401	0.17 ± 0.01	0.29 ± 0.01	16.74 ± 0.01	2.79 ± 0.01	19.2 ± 0.01	0.691 ± 0.004	58.8 ± 1.7
5050020204	1.16 ± 0.02	1.01 ± 0.01	12.2 ± 0.02	5.58 ± 0.02	18.94 ± 0.02	$0.694^{+0.005}_{-0.001}$	$50.7^{+1.2}_{-1.1}$
5050020206	15.99 ± 0.04	14.6 ± 0.02	2.53 ± 0.03	16.66 ± 0.03	42.02 ± 0.03	0.684 ± 0.002	42.5 ± 0.7
5050020208	2.35 ± 0.02	0.43 ± 0.01	15.55 ± 0.02	8.1 ± 0.01	24.93 ± 0.02	0.688 ± 0.002	48.4 ± 2.7
5050020221	12.66 ± 0.04	11.51 ± 0.02	1.45 ± 0.02	17.78 ± 0.03	37.25 ± 0.03	$0.684^{+0.005}_{-0.003}$	44.7 ± 1.4
5050020222	0.65 ± 0.01	1.22 ± 0.01	13.4 ± 0.02	4.16 ± 0.01	18.17 ± 0.02	$0.697^{+0.002}_{-0.004}$	50.5 ± 1.0

Appendix C
NuSTAR Fit Parameters

This section of the appendix summarizes the results of reflection modeling for the NuSTAR spectra. Table C1 contains the fit parameters for a reflection model applied to the NuSTAR spectra alone. Note: † indicates the parameter reached an upper bound and had no constraints on uncertainty.

Table C1
4U 0614+091 Results of Reflection Modeling: NuSTAR

		30363002002	30702009002	30702009004	30702009006	30702009008	30702009010
CONSTANT	const	$0.968^{+0.004}_{-0.003}$	1.00 ± 0.01	$0.996^{+0.006}_{-0.004}$	$0.995^{+0.006}_{-0.004}$	0.996 ± 0.001	0.98 ± 0.01
BBODY	kT (keV)	$1.55^{+0.02}_{-0.03}$	$1.16^{+0.03}_{-0.04}$	$1.07^{+0.03}_{-0.06}$	$0.65^{+0.07}_{-0.04}$	$1.16^{+0.01}_{-0.02}$	$1.06^{+0.01}_{-0.03}$
	$k_{\rm BB}$ (10^{-3})	$6.1^{+0.4}_{-0.1}$	2.2 ± 0.3	$1.5^{+0.1}_{-0.2}$	$1.50^{+0.02}_{-0.38}$	1.6 ± 0.1	$1.46^{+0.04}_{-0.19}$
DISKBB	kT (keV)	0.2 ± 0.2	$0.50^{+0.02}_{-0.04}$	$0.49^{+0.01}_{-0.07}$	$1.7^{+0.2}_{-0.5}$	$0.58^{+0.02}_{-0.05}$	$0.54^{+0.01}_{-0.02}$
	$k_{\rm DBB}$	$1117.4^{+1854.3}_{-1045.9}$	$274.2^{+118.7}_{-70.5}$	$388.8^{+264.2}_{-73.8}$	$0.3^{+0.5}_{-0.3}$	$100.3^{+68.5}_{-27.7}$	$172.3^{+19.3}_{-19.8}$
CUTOFFPL	Γ	$2.15^{+0.06}_{-0.03}$	$2.15^{+0.02}_{-0.08}$	$2.04^{+0.07}_{-0.04}$	$1.84^{+0.12}_{-0.01}$	$2.15^{+0.01}_{-0.02}$	$2.06^{+0.04}_{-0.01}$
	$E_{\rm cutoff}$ (keV)	$10.1^{+0.5}_{-0.4}$	$100.7^{+8.7}_{-22.0}$	$119.7^{+30.6}_{-14.7}$	$85.9^{+60.4}_{-4.1}$	$121.7^{+12.7}_{-23.0}$	$199.0^{+0.9}_{-27.7}$
	$k_{\rm PL}$	$0.48^{+0.13}_{-0.04}$	$0.19^{+0.01}_{-0.05}$	$0.16^{+0.04}_{-0.03}$	$0.09^{+0.04}_{-0.01}$	0.20 ± 0.01	0.24 ± 0.01
RELCONV	q	2.0 ± 1.0	$0.52^{+0.06}_{-0.04}$	$2.0^{+1.2}_{-1.0}$	$2.9^{+1.7}_{-1.1}$	$2.2^{+0.2}_{-0.3}$	$3.0^{+0.2}_{-0.3}$
	$R_{\rm in}$ ($R_{\rm ISCO}$)	$4.2^{+6.3}_{-2.1}$	$19.8^{+0.2}_{-3.5}$	$3.6^{+4.3}_{-2.6}$	$6.8^{+9.8}_{-5.1}$	2.2 ± 1.0	$3.4^{+0.3}_{-0.5}$
XILLVERCO	A_{CO}	$52.0^{+8.8}_{-11.1}$	$1.0^{\dagger}$	$3.0^{+9.2}_{-1.9}$	$38.8^{+14.8}_{-9.1}$	$7.3^{+4.0}_{-3.3}$	$17.1^{+16.1}_{-4.5}$
	frac	0.5 ± 0.1	$0.14^{+0.04}_{-0.02}$	$0.10^{+0.01}_{-0.02}$	$0.09^{+0.07}_{-0.02}$	0.12 ± 0.01	$0.056^{+0.015}_{-0.001}$
	$kT_{\rm xill}(10^{-2}$ keV)	$8.8^{+0.1}_{-1.0}$	$8.1^{+0.6}_{-0.8}$	$8.0^{+1.3}_{-0.3}$	$8.4^{+0.1}_{-0.9}$	$8.9^{+0.2}_{-0.4}$	$7.5^{+0.8}_{-0.4}$
	$k_{\rm xillverCO}$ (10^{-9})	2.1 ± 0.4	$3.0^{+1.0}_{-0.7}$	$3.5^{+0.8}_{-1.2}$	$4.6^{+1.4}_{-1.3}$	$2.9^{+0.1}_{-0.2}$	$8.4^{+0.1}_{-0.5}$
	$\log \xi$	3.6 ± 0.1	2.9 ± 0.2	2.7 ± 0.2	2.8 ± 0.4	3.0 ± 0.1	2.4 ± 0.1
	χ^2(dof)	236(193)	218(210)	221(210)	215(212)	248(211)	226(215)

ORCID iDs

D. L. Moutard https://orcid.org/0000-0003-1463-8702
R. M. Ludlam https://orcid.org/0000-0002-8961-939X
E. M. Cackett https://orcid.org/0000-0002-8294-9281
J. A. García https://orcid.org/0000-0003-3828-2448
J. M. Miller https://orcid.org/0000-0003-2869-7682
D. R. Wilkins https://orcid.org/0000-0002-4794-5998

References

Arnason, R. M., Papei, H., Barmby, P., Bahramian, A., & D. Gorski, M. 2021, MNRAS, 502, 5455
Arnaud, K. A. 1996, in ASP Conf. Ser. 101, Astronomical Data Analysis Software and Systems V, ed. G. H. Jacoby & J. Barnes (San Francisco, CA: ASP), 17
Avakyan, A., Neumann, M., Zainab, A., et al. 2023, A&A, 675, A199
Bahramian, A., & Degenaar, N. 2023, in Handbook of X-Ray and Gamma-Ray Astrophysics, ed. C. Bambi & A. Santangelo (Singapore: Springer), 120
Bhattacharyya, S., & Strohmayer, T. E. 2007, ApJL, 664, L103
Brandt, S., Castro-Tirado, A. J., Lund, N., et al. 1992, A&A, 262, L15
Buisson, D. J. K., Fabian, A. C., Barret, D., et al. 2019, MNRAS, 490, 1350
Cackett, E. M., Miller, J. M., Ballantyne, D. R., et al. 2010, ApJ, 720, 205
Chen, W.-C., Liu, D.-D., & Wang, B. 2020, ApJL, 900, L8
Churazov, E., Gilfanov, M., Forman, W., & Jones, C. 1996, ApJ, 471, 673
Dauser, T., García, J., Walton, D. J., et al. 2016, A&A, 590, A76
Degenaar, N., Ballantyne, D. R., Belloni, T., et al. 2018, SSRv, 214, 15
Done, C., Gierliński, M., & Kubota, A. 2007, A&ARv, 15, 1
Fabian, A. C., Rees, M. J., Stella, L., & White, N. E. 1989, MNRAS, 238, 729
García, J., Dauser, T., Reynolds, C. S., et al. 2013, ApJ, 768, 146
García, J. A., Dauser, T., Ludlam, R., et al. 2022, ApJ, 926, 13
García, J. A., Steiner, J. F., McClintock, J. E., et al. 2015, ApJ, 813, 84
Ibragimov, A., & Poutanen, J. 2009, MNRAS, 400, 492
Juett, A. M., Psaltis, D., & Chakrabarty, D. 2001, ApJL, 560, L59
Kaastra, J. S., & Bleeker, J. A. M. 2016, A&A, 587, A151
Kara, E., Steiner, J. F., Fabian, A. C., et al. 2019, Natur, 565, 198
Koliopanos, F., Gilfanov, M., & Bildsten, L. 2013, MNRAS, 432, 1264
Koliopanos, F., Vasilopoulos, G., Guillot, S., & Webb, N. 2021, MNRAS, 500, 5603
Krawczynski, H., Muleri, F., Dovciak, M., et al. 2022, Sci, 378, 650
Lin, D., Remillard, R. A., & Homan, J. 2007, ApJ, 667, 1073
Long, M., Romanova, M. M., & Lovelace, R. V. E. 2005, ApJ, 634, 1214
Ludlam, R., Miller, J. M., Cackett, E., et al. 2016, AAS, HEAD meeting, 15, 120.14
Ludlam, R. M. 2024, Ap&SS, 369, 16
Ludlam, R. M., Cackett, E. M., García, J. A., et al. 2020, ApJ, 895, 45
Ludlam, R. M., Miller, J. M., Barret, D., et al. 2019, ApJ, 873, 99
Madej, O. K., Garcia, J., Jonker, P. G., et al. 2014, MNRAS, 442, 1157
Madej, O. K., & Jonker, P. G. 2011, MNRAS, 412, L11
Matsuoka, M., Kawasaki, K., Ueno, S., et al. 2009, PASJ, 61, 999
Migliari, S., Tomsick, J. A., Miller-Jones, J. C. A., et al. 2010, ApJ, 710, 117
Miller, J. M., D'Aì, A., & Bautz, M. W. 2010, ApJ, 724, 1441
Moutard, D. L., Ludlam, R. M., García, J. A., et al. 2023, ApJ, 957, 27
Nelemans, G., Jonker, P. G., Marsh, T. R., & van der Klis, M. 2004, MNRAS, 348, L7
Nelemans, G., Jonker, P. G., & Steeghs, D. 2006, MNRAS, 370, 255
Ng, C., Díaz Trigo, M., Cadolle Bel, M., & Migliari, S. 2010, A&A, 522, A96
Parikh, A. S., Wijnands, R., Degenaar, N., et al. 2017, MNRAS, 466 4074
Pinto, C., Kaastra, J. S., Costantini, E., & de Vries, C. 2013, A&A, 551, A25
Savonije, G. J., de Kool, M., & van den Heuvel, E. P. J. 1986, A&A, 155, 51
Shahbaz, T., Watson, C. A., Zurita, C., Villaver, E., & Hernandez-Peralta, H. 2008, PASP, 120, 848
Shakura, N. I., & Sunyaev, R. A. 1973, A&A, 24, 337

Sibgatullin, N. R., & Sunyaev, R. A. 2000, AstL, 26, 699
Swank, J. H., Becker, R. H., Boldt, E. A., Holt, S. S., & Serlemitsos, P. J. 1978, MNRAS, 182, 349
Syunyaev, R. A., Arefev, V. A., Borozdin, K. N., et al. 1991, SvAL, 17 409
Tanaka, Y., Nandra, K., Fabian, A. C., et al. 1995, Natur, 375, 659
Tomsick, J. A., Yamaoka, K., Corbel, S., et al. 2009, ApJL, 707, L87
Verner, D. A., Ferland, G. J., Korista, K. T., & Yakovlev, D. G. 1996, ApJ, 465, 487
Wilkins, D. R. 2018, MNRAS, 475, 748
Wilkins, D. R., & Fabian, A. C. 2012, MNRAS, 424, 1284
Wilkins, D. R., Kara, E., Fabian, A. C., & Gallo, L. C. 2014, MNRAS, 443, 2746
Wilms, J., Allen, A., & McCray, R. 2000, ApJ, 542, 914